

SOLID STATE PHYSICS

PART IV

Superconducting Properties of Solids

M. S. Dresselhaus

Contents

| | | |
|----------|---|-----------|
| 1 | Superconducting Properties of Solids | 1 |
| 1.1 | Perfect Conductivity $R = 0$ (1911) | 1 |
| 1.2 | Meissner Effect $B = 0$ | 3 |
| 1.2.1 | Critical Fields | 4 |
| 1.3 | Flux Quantization | 4 |
| 1.4 | The Superconducting Energy Gap | 7 |
| 1.5 | Thermal Conductivity | 7 |
| 1.6 | Quasi-particle Tunneling | 9 |
| 1.7 | Isotope Effect | 12 |
| 1.8 | Thermodynamics of Superconductors | 12 |
| 1.9 | Microscopic Description of Superconductivity | 14 |
| 2 | Macroscopic Quantum Description of Superconductivity | 15 |
| 2.1 | The Cooper Pair | 15 |
| 2.2 | Macroscopic Quantum Description of the Supercurrent | 17 |
| 2.3 | The Quantum Mechanical Current | 18 |
| 2.4 | The Supercurrent Equation | 19 |
| 2.5 | The London Equations | 20 |
| 2.6 | The Two-Fluid Model | 21 |
| 2.7 | Flux Quantization | 23 |
| 2.8 | The Vortex Phase and Trapped Flux | 24 |
| 2.9 | Summary of Length Scales | 26 |
| 2.10 | Weakly-Coupled Superconductors – The Josephson Effect | 27 |
| 2.11 | Effect of Magnetic Fields on Josephson Junctions – Superconducting Quantum Interference | 31 |
| 2.12 | Quantum Interference Between Two Junctions | 31 |
| 3 | Microscopic Quantum Description of Superconductivity | 34 |
| 3.1 | Bardeen-Cooper-Schrieffer (BCS) Theory | 34 |
| 3.1.1 | The Cooper Instability | 34 |
| 3.1.2 | Ground State From Cooper Pairs | 37 |
| 3.1.3 | Hamiltonian for the Superconducting Ground State | 37 |
| 3.1.4 | Superconducting Ground State | 40 |
| 3.1.5 | Long-range Coherence | 42 |
| 3.2 | Gap Parameter and Condensation Energy at $T = 0$ | 42 |
| 3.2.1 | Condensation Energy | 43 |

| | | |
|----------|---|-----------|
| 3.3 | Some Quantitative Predictions of BCS | 44 |
| 3.3.1 | Critical Temperature | 44 |
| 3.3.2 | Energy Gap | 44 |
| 3.3.3 | Critical Field | 45 |
| 3.3.4 | Specific Heat | 46 |
| 4 | Superconductivity in High Transition Temperature Cuprate Materials | 47 |
| 4.1 | Introduction to High T_c Materials | 47 |
| 4.2 | Anisotropic Superconducting Properties | 52 |
| 4.3 | Anisotropic Normal State Transport Properties | 56 |
| 4.4 | The Hall Effect in High T_c Materials | 60 |

Chapter 1

Superconducting Properties of Solids

References:

- Ashcroft and Mermin, *Solid State Physics*, Chapter 34.
- Kittel, *Introduction to Solid State Physics*, 6th Ed., Chapter 12.
- T. van Duzer and C.W. Turner, *Principles of Superconductive Devices and Circuits*, Elsevier, NY (1981).
- M. Tinkham, *Introduction to Superconductivity*, McGraw-Hill, 1975.
- T.P. Orlando, *Foundations of Applied Superconductivity*, Addison–Wesley, 1991.

Superconductors exhibit a unique set of properties. These unique properties are summarized in this chapter.

1.1 Perfect Conductivity $R = 0$ (1911)

The resistance of a normal metal gradually decreases as the temperature is lowered and levels off at very low temperatures (see Fig. 1.1). The resistance at absolute zero is determined by electrons scattered by impurities and defects in the metal (see §7.3 of part I). Many metals, however, undergo a phase transition to the superconducting state (see Fig. 1.1), whereby these metals have zero resistance below some temperature, T_c , the **superconducting transition temperature** (see Fig. 1.1). The phase transition to a superconducting phase effect was discovered by Kamerlingh Onnes in 1911, shortly after he had for the first time liquefied helium (boiling point = 4.2 K). Some typical T_c 's for elemental superconductors are 9.25 K for Niobium (Nb), 7.2 K for lead (Pb), 1.1 K for Al, and even silicon is superconducting under pressure at 7.1 K! Some typical T_c 's for important elemental superconductors are given in Table 1.1. However, noble metals like copper (Cu), gold (Au) and silver (Ag) have not yet been found to undergo a superconducting transition for temperatures as low as a few millidegrees Kelvin. Until 1986, the highest known transition temperature was 23.2 K for Nb₃Ge. This is one reason why the scientific community was so surprised by the discovery

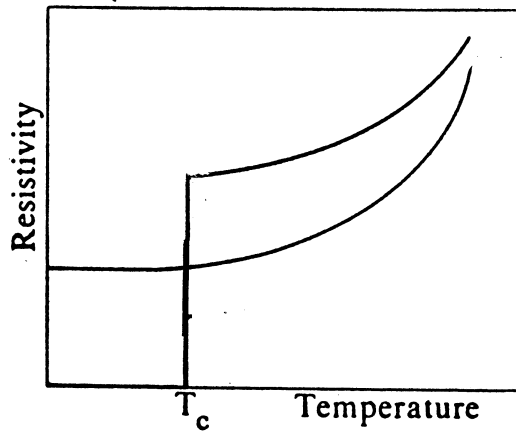


Figure 1.1: Low temperature resistance of a typical normal metal (upper curve), showing a dc resistivity at low temperatures of the form $\rho = \rho_0 + AT^5$ and a superconductor (lower curve), showing zero resistivity below the superconducting transition temperature T_c .

Table 1.1: Superconducting transition temperatures (T_c) and critical magnetic fields (H_c) for some typical elemental superconductors.

| Material | T_c (K) | H_c (gauss) |
|----------|-----------|---------------|
| Al | 1.1 | 99 |
| Sn | 3.7 | 305 |
| Pb | 7.2 | 803 |
| Nb | 9.25 | 1980 |
| Hg | 4.15 | 411 |
| V | 5.38 | 1020 |
| In | 3.4 | 293 |
| La | 4.9 | 798 |
| Ta | 4.48 | 830 |
| Tc | 7.77 | 1410 |
| Pa | 1.4 | – |
| Re | 1.7 | 198 |
| Tl | 2.39 | 171 |

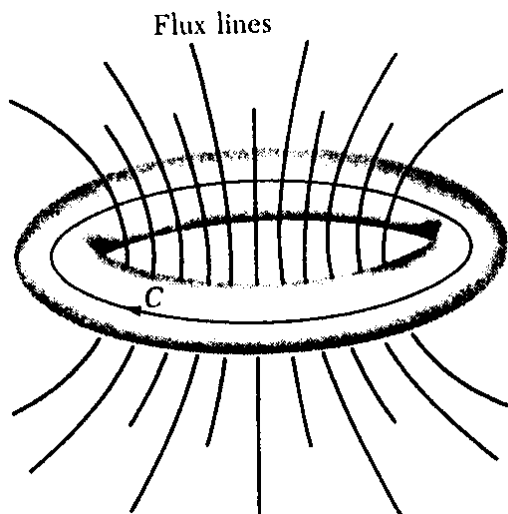


Figure 1.2: A superconducting ring showing persistent current threaded by magnetic lines of flux.

in 1986 of high T_c superconductivity in transition metal cuprate compounds, with T_c values far exceeding the previous record of 23.2 K, and by 1987 T_c values of > 120 K were reported, ushering in a new period of high research activity on high T_c superconducting materials.

An interesting consequence of perfect conductivity is that if a current is introduced into a ring of a superconducting material, then the current will persist indefinitely, without decaying (see Fig. 1.2). On the other hand, the current carrying capacity of a superconductor is finite and cannot exceed a critical current density j_c , above which it reverts back to the normal state.

1.2 Meissner Effect $B = 0$

Besides perfect conductivity, the other main characteristic of superconductivity is perfect diamagnetism; this means that $B = 0$ within a superconductor and that magnetic flux is excluded from a superconductor. This fundamental property of superconductors was first identified by Meissner in 1933 and is called the Meissner effect. In Fig. 1.3 we see the magnetic field lines for a perfect conductor (a) and for a perfect diamagnet (b), which is a superconductor. We shall see later that there is, in fact, an exponential decay of the magnetic flux at the surface of a superconductor $e^{-z/\lambda}$, and this decay is characterized by the superconducting penetration depth λ .

As shown in Fig. 1.3, no flux penetrates a superconductor for $T < T_c$ and $H < H_c$, whether it is cooled in a magnetic field or not. In contrast, a perfect conductor will have no flux inside, only if it is cooled below T_c in zero field. This is evidence that **a superconductor is more than a perfect conductor**.

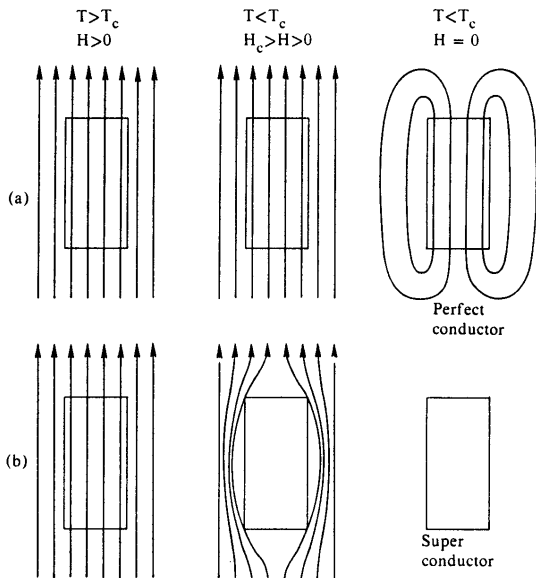


Figure 1.3: Schematic diagram of the magnetic field behavior of (a) a “perfect electrical conductor” defined as a normal metal having zero resistance below T_c , and (b) a metal that is a superconductor below T_c . The lines with arrows indicate the magnetic flux lines. Whereas the normal metal has no flux exclusion, a superconductor exhibits full flux exclusion.

1.2.1 Critical Fields

If an external magnetic field is increased above a critical value (see Table 1.1), the superconductor will revert to the normal state with finite resistivity. For type I superconductors, B remains zero until the sample exceeds the critical field H_c (see Fig. 1.4a). Most elemental superconductors are Type-I superconductors and exhibit low critical fields (see Fig. 1.5a) and a simple magnetization curve (see Fig. 1.6a). For a Type II superconductor, B remains zero only for relatively small magnetic fields ($H < H_{c1}$) (see Fig. 1.4b). Then above this critical field value (H_{c1}), magnetic flux enters the superconductor in the form of vortices (see Figs. 1.4b and 1.6b). These vortices have a core of material in the normal state, around which super-currents circulate. As the magnetic field increases, the density of vortices increases until the upper critical field H_{c2} is reached, where the vortex cores (which are in the normal phase) overlap with one another, and the material becomes a normal metal completely (see Figs. 1.4b and 1.6b). Most materials of practical interest are type II superconductors where typical values of H_{c2} are in the Tesla range (see Figs. 1.5a,b). The critical parameters that characterize a type II superconductor are T_c , H_{c2} and j_c , where j_c is the critical current density. For current densities above j_c , superconductivity is destroyed and the normal resistive state is restored. For practical applications it is desirable for all three critical parameters (T_c , H_{c2} , j_c) to be large.

1.3 Flux Quantization

When a persistent (non-decaying) current is induced in a superconducting ring (see Fig. 1.2), the resulting flux within the ring is found to be quantized in units of $\Phi_0 = ch/2e = 2.0678 \times 10^{-7} \text{ gauss cm}^2 = 2.0678 \times 10^{-15} \text{ tesla-m}^2$. The experimental confirmation of flux quantization in superconductor rings was first reported by 2 experimental groups in 1961

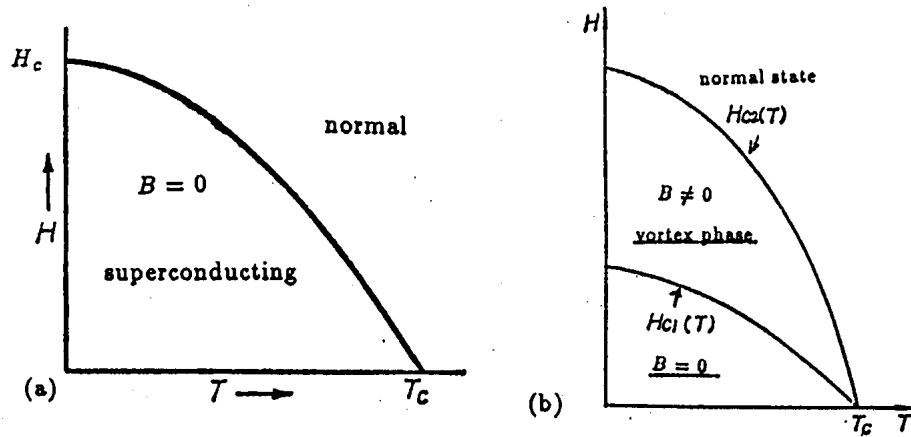


Figure 1.4: Schematic magnetic phase diagrams of (a) type I and (b) type II superconductors. Note the formation of a vortex phase above H_{c1} in a type II superconductor, where magnetic flux penetrates into the core of the vortices.

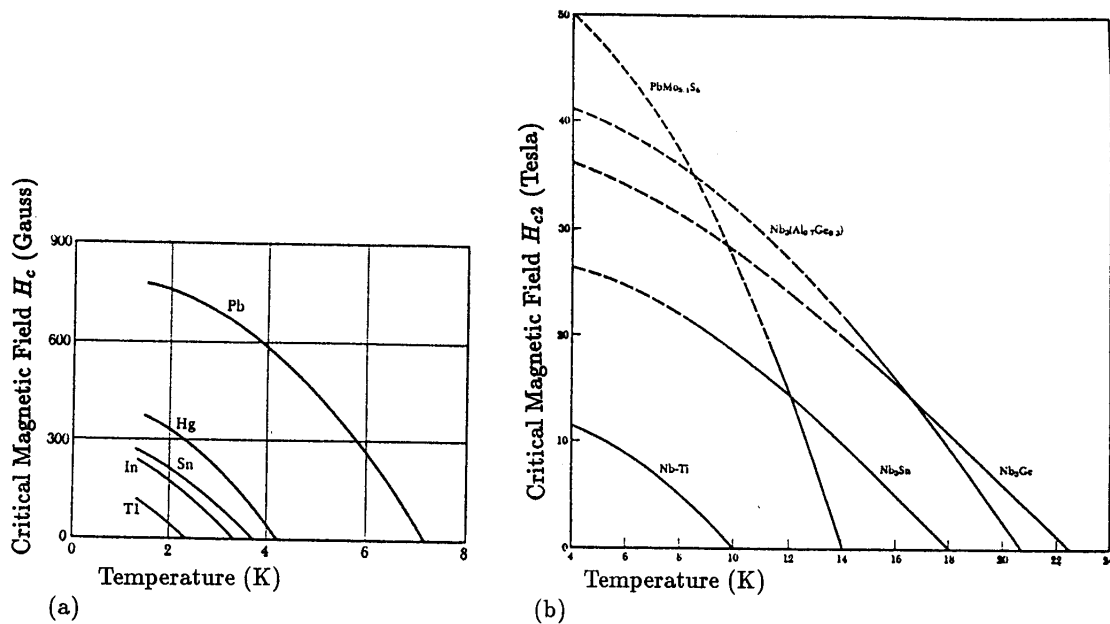


Figure 1.5: (a) Plot of H_c vs T for several type I superconductors. (b) Plot of H_{c2} vs T for several type II superconductors. Notice the great difference in scale for the critical fields between type I and type II superconductors. Because of their high critical fields, Type II superconductors are of particular interest for superconducting magnet applications.

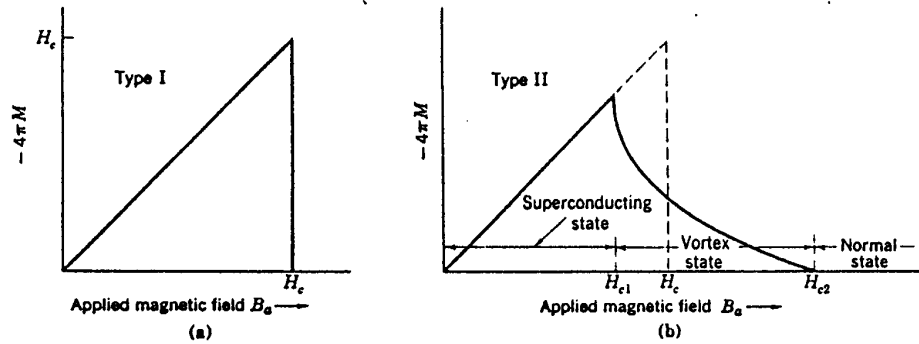


Figure 1.6: (a) Magnetization versus applied magnetic field for a bulk superconductor exhibiting a complete Meissner effect, i.e., perfect diamagnetism. A superconductor with this behavior is called a type I superconductor. Above the critical field H_c the specimen becomes a normal conductor and the magnetization is too small to be seen on this scale. Note that $-4\pi M$ is plotted on the vertical scale (a negative value for the magnetic susceptibility corresponds to diamagnetism). (b) Magnetization curve of a type II superconductor. The flux starts to penetrate the specimen at a field H_{c1} which is lower than the thermodynamic critical field H_c . The specimen is in a vortex state between H_{c1} and H_{c2} , but has superconducting electrical properties up to H_{c2} . For a given type II superconductor, the area under the dashed magnetization curve in (b) is the same for a type II superconductor as for a type I superconductor.

(B.S. Deaver and W.M. Fairbank, Phys. Rev. Lett. **7**, 43 (1961) and R. Doll and M. Näbauer, Phys. Rev. Lett. **7**, 51 (1961)). This observation strongly suggested that **superconductivity is a quantum mechanical phenomenon**. As a consequence of flux quantization, there are vortices in type II superconductors, and each vortex encloses a single quantized unit of flux Φ_0 .

1.4 The Superconducting Energy Gap

Prior to the discovery of flux quantization, experiments on the heat capacity and on the absorption of microwave power were performed, each of which provided evidence for an energy gap, characteristic of the superconducting state. These two experiments were critical to the development of the microscopic theory of superconductivity. The existence of an energy gap was soon verified experimentally by the elegant tunneling experiments by Giaever (see § 1.6).

The heat capacity C of a material is the amount of heat ΔQ needed to raise the temperature by $\Delta T = 1$ K per mole, namely $\Delta Q = C\Delta T$. For normal metals the heat capacity exhibits a temperature dependence $C = \gamma T + \beta T^3$. The first term ($C_e = \gamma T$) arises from the electronic contribution, while the second term ($C_L = \beta T^3$) arises from the lattice. At low temperatures the specific heat is dominated by the electronic part, $C_e = \gamma T$. As a metal is cooled below the transition temperature T_c , the electronic part of the heat capacity of a superconductor, increases abruptly and then decays rapidly with decreasing temperature (see Fig. 1.7), falling off to zero exponentially as $T \rightarrow 0$. Such an exponential fall-off in $C(T)$ provided early evidence (1954) for an **energy gap**, Δ (see Fig. 1.7).

The microwave absorption experiment likewise provided direct evidence for an energy gap, including an early determination of the temperature dependence of the energy gap $\Delta(T)$ (see Fig. 1.8). In §1.8 we present a simple model for the thermodynamics of superconductors, which provides background for the heat capacity studies of Fig. 1.7, while in § 2.5 we present the London equations, describing the electromagnetics of superconductors, which is based on a two-fluid model for superconductivity (see §2.6). According to this model the electrons in a superconductor consist of superconducting electrons with no resistance and normal electrons which can dissipate energy at ac (microwave) frequencies.

1.5 Thermal Conductivity

In our study of transport properties (see part I, §6.2.2) we found that for metals, the electronic contribution κ_e dominates the thermal conductivity $\kappa = \kappa_e + \kappa_L$. For normal metals, κ_e is proportional to the electron density. However, for a superconductor at $T = 0$, the electrons are all in the superconducting state, bound in Cooper pairs, as we discuss in §2.1. When the electrons are all bound in pairs, they do not contribute to κ , because they are in a fully ordered state and have no entropy. Thus at finite temperatures, κ for a superconductor is very small (see Fig. 1.9), since only the excited quasiparticles of the two fluid model (as discussed below) can contribute to κ . The low thermal conductivity of superconductors for $T \ll T_c$, can be utilized in a low temperature heat switch. Application of a magnetic field can be used to cause a superconducting-normal transition, thereby restoring high thermal conductivity and a good thermal conduction path to the metal.

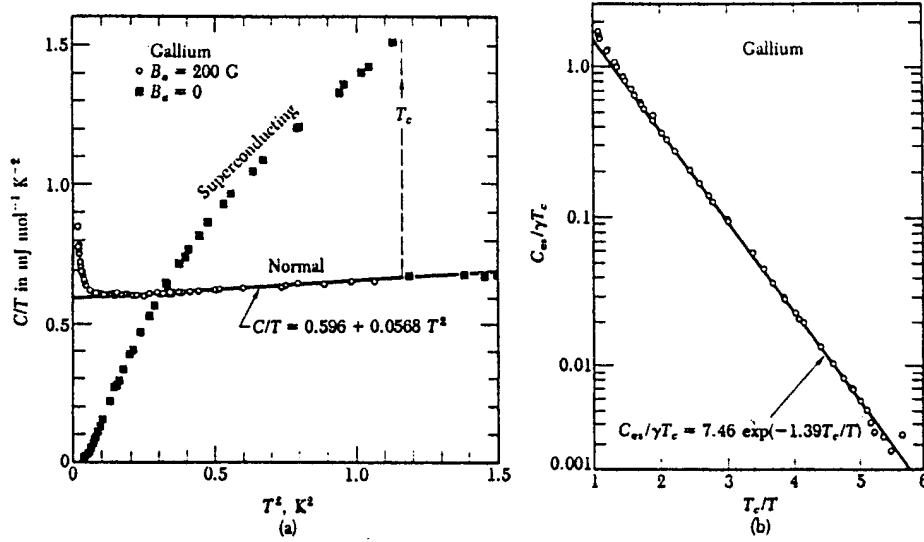
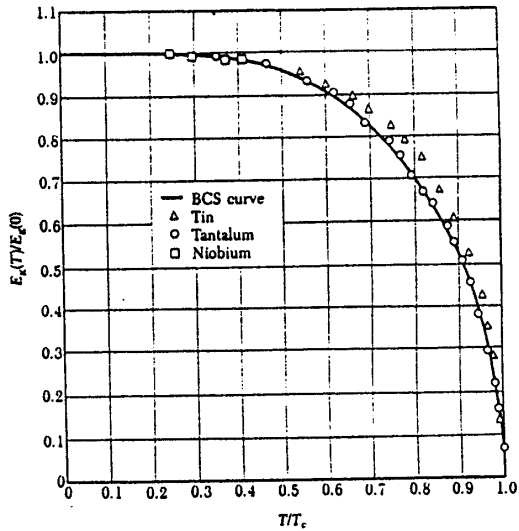


Figure 1.7: (a) The heat capacity of gallium in the normal and superconducting states. The normal state (which is restored by a 200 G magnetic field) has electronic, lattice and (at low temperatures) nuclear quadrupole contributions to the heat capacity. In (b) the electronic part C_{el} of the heat capacity in the superconducting state is plotted on a log scale versus T_c/T : the exponential dependence of $C(T)$ on $1/T$ at low temperature is evident in the figure. (The coefficient $\gamma = 0.60 \text{ mJ mol}^{-1} \text{ deg}^2$ for Ga).

Figure 1.8: The reduced values of the observed energy gap $E_g(T)/E_g(0)$ as a function of reduced temperature T/T_c for several superconductors. The solid curve is drawn for the BCS theory of superconductivity.



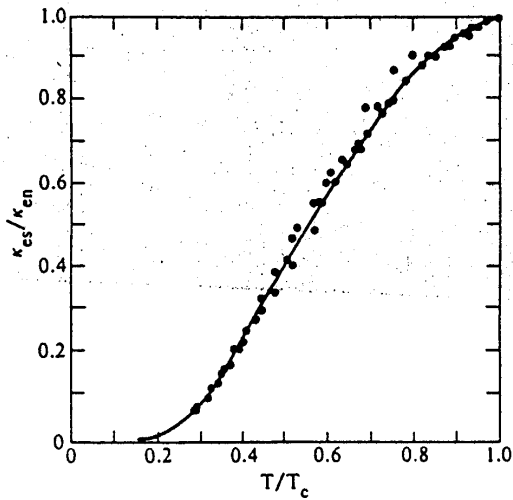


Figure 1.9: Ratio of the electronic thermal conductivity in the superconducting state to that in the normal state of aluminum (dots) as a function of temperature. The curve is calculated from the BCS theory of superconductivity, and shows the poor thermal conductivity of superconductors at low temperatures.

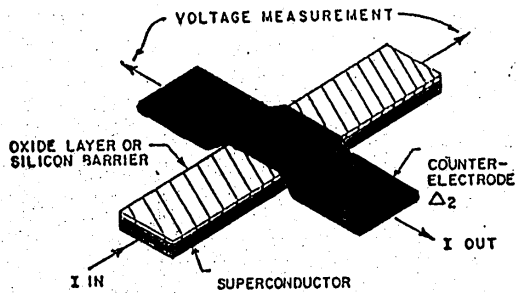


Figure 1.10: Superconducting tunnel junction which consists of a superconductor-insulator-superconductor (S/I/S) sandwich, where tunneling occurs between the two superconducting layers (S) which are in black and an oxide layer is used as an insulator (I) between them.

1.6 Quasi-particle Tunneling

Measurements of the properties of the superconducting energy gap were greatly facilitated by the observation of tunneling in a superconductor. In this section, we explain quasiparticle tunneling in a superconductor and show how measurement of the $I - V$ characteristics of the tunnel junction yields information on the superconducting energy gap. The structure of a tunnel junction is shown in Fig. 1.10. Classical physics, of course, would say that no current could pass through the insulating barrier in Fig. 1.10. However, the quantum mechanical nature of the electrons allows them to tunnel through a thin insulating barrier.

Two types of tunneling can, in fact, occur if the counter-electrode is also a superconductor. The first is quasiparticle tunneling which was discovered by Giaever in 1960 and is discussed in this section, and the second type of tunneling is Josephson tunneling discovered by Josephson in 1962, and discussed in §2.10. Both of these discoveries were made by two very young men, before either had completed their Ph.D. theses.

In the quasiparticle tunneling experiments, “electrons” tunnel through the insulating layers of the S/I/S sandwich of Fig. 1.10 until their energy exceeds the gap energy, above

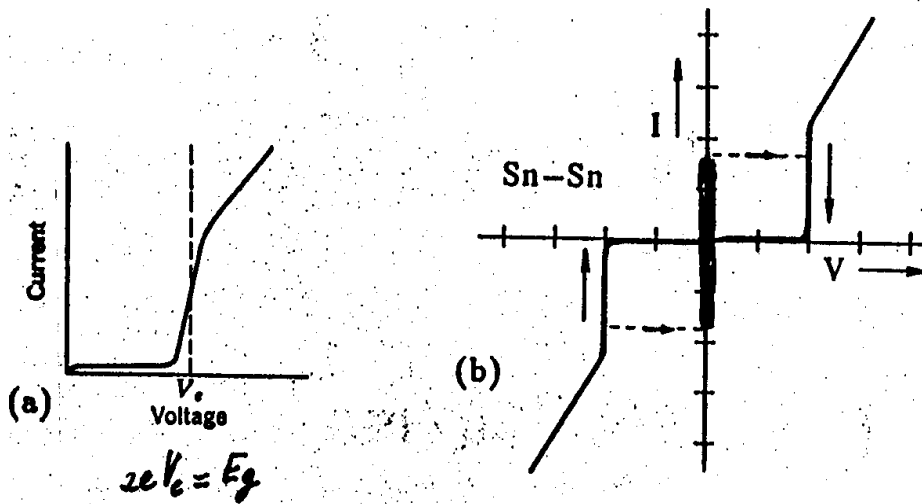


Figure 1.11: $I - V$ characteristics for (a) quasiparticle tunneling in a tunnel junction for a S/I/S device (see Fig. 1.10), and (b) Josephson tunneling through a weak link Josephson tunnel junction.

which the $I - V$ curve follows Ohm's law (see Fig. 1.11a). In Josephson tunneling (see Fig. 1.11b), a superconducting current can flow at zero voltage until the current reaches a critical current I_c , above which the $I - V$ curve switches to the resistive part of the tunnel-junction characteristic and again follows Ohm's law (see §2.10).

Once quasiparticle tunneling was discovered, it became the standard method for measuring the superconducting energy gap and the dependence of the gap on temperature and magnetic field. The insulator in Fig. 1.10 normally acts as a barrier to the flow of conduction electrons from one metal to the other. If the barrier is sufficiently thin (less than 10 or 20 Å), there is a significant probability that if a voltage is applied across the S/I/S device, an electron which impinges on the insulating barrier will tunnel from one metal electrode to the other.

When both metals are normal conductors (M), the current-voltage relation of the M/I/M sandwich or tunneling junction is ohmic at low voltages, with the current directly proportional to the applied voltage. Giaever (1960) discovered that if one of the metals becomes superconducting (S), the current-voltage characteristic of the M/I/S sandwich changes from the linear Ohmic behavior of Fig. 1.12(a) to the curve shown in Fig. 1.12(b). Giaever explained his observation in terms of the model of the density of states shown in Fig. 1.12(b) for the superconductor.

Figure 1.12(b) contrasts the electron density of states in the superconductor with that in the normal metal, shown in Fig. 1.12(a). In the superconductor there is an energy gap centered at the Fermi level. The electron states that had been in the energy gap range (in the normal state), now pile up on either side of the energy gap, giving a very high density of states in the regions adjacent to the energy gap, and shown in Fig. 1.12(b). From the microscopic theory of superconductivity it is known that quasiparticle tunneling involves

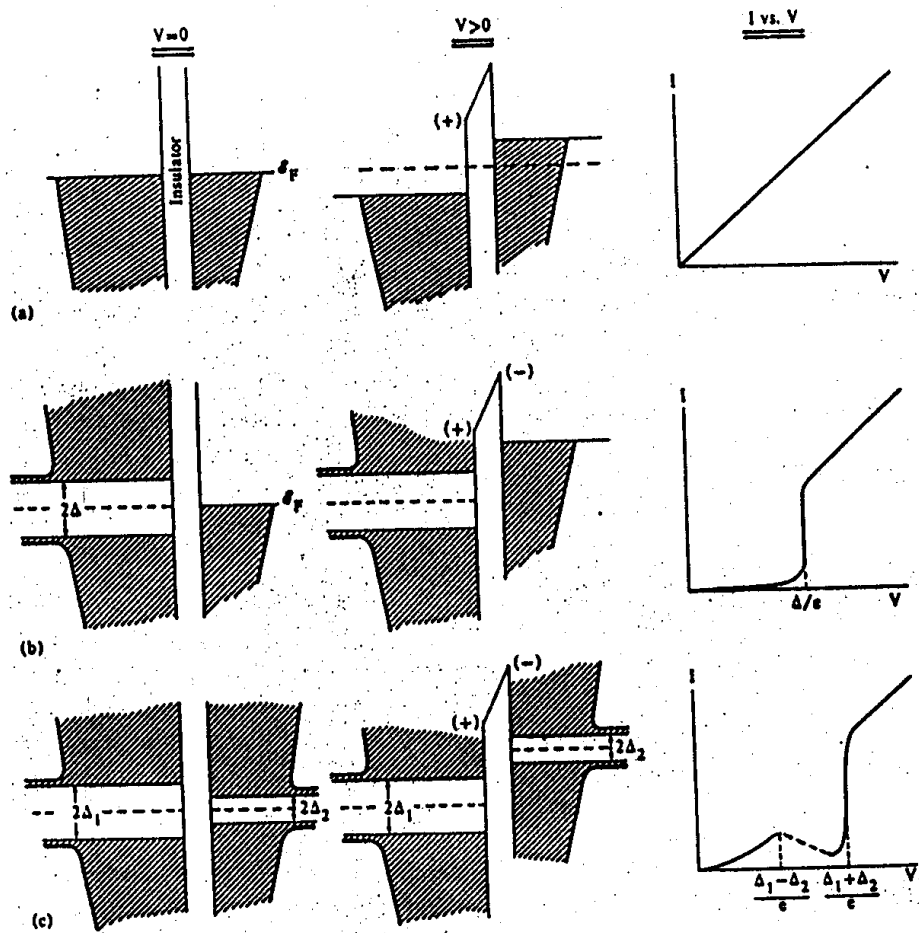


Figure 1.12: The six density of states versus energy diagrams on the left are for $T = 0\text{K}$ and the three diagrams on the right are all plots of the current versus voltage for the various types of metals on the left. (a) This shows two normal metals separated by a thin insulating film with zero applied voltage and then for $V > 0$. (b) The same situation as (a) but now one of the metals is a superconductor. (c) Now both of the metals are superconductors with different gaps. (E_F is the Fermi energy.)

a pair of electrons (see §2.1) rather than a single electron, as in the case of tunneling in a normal metal.

Since an electron pair is involved, the current in the M/I/S sandwich starts to flow at $T = 0\text{K}$ when $eV = \Delta$ where Δ is half the energy gap (see Fig. 1.12b). At finite temperatures there is a small current flow even at lower voltages, because of electrons in the superconductor that are thermally excited across the energy gap. Clearly Fig. 1.12b shows that quasiparticle tunneling provides a direct method for measuring the superconducting energy bandgap.

Also of interest is case (c) of Fig. 1.12 for tunneling in a S/I/S junction, where the metals on either side of the tunnel barrier are superconducting. Near $T = 0$ all the electrons in the small gap superconductor [Fig. 1.12(c)] are paired and there are few excited electrons. Thus, it is only when the bias voltage exceeds $(\Delta_1 + \Delta_2)/e$ that there is a significant density of electrons to tunnel across the barrier. For bias voltages less than $(\Delta_1 - \Delta_2)/e$, only the low density of thermally excited electrons from the small gap superconductor can tunnel into the wide gap superconductor, so that only a small amount of tunneling occurs. In this case, I increases until $V = (\Delta_1 - \Delta_2)/e$ is reached where the joint density of states is maximized. As the voltage is increased from $(\Delta_1 - \Delta_2)/e$ to $(\Delta_1 + \Delta_2)/2$, the joint density of states available for tunneling decreases and the tunneling current consequently also decreases. By increasing the temperature above T_c or increasing the magnetic field above H_{c2} , the small bandgap material will go normal, and case (b) is reached. Thus when two superconductors are used, it is possible to get information on the bandgaps of both superconductors.

1.7 Isotope Effect

The first clue to the microscopic origin of superconductivity came from studying metals containing different isotopes of a particular elemental superconductor. In these experiments, the superconducting transition temperature T_c was found to decrease with increasing isotopic mass according to the relation

$$M^\alpha T_c = \text{constant}, \quad (1.1)$$

where $\alpha \simeq 1/2$. The discovery of the isotope effect was totally unexpected and indicated that superconductivity involved a strong interaction (electron-phonon coupling) between the electrons and the lattice.

1.8 Thermodynamics of Superconductors

In order to increase our understanding of the temperature dependence of the specific heat of superconductors and the nature of the normal-superconducting phase transition, we consider in this section a simple model for the thermodynamics of a metal in the normal state and in the superconducting state.

The Gibbs free energy per unit volume of a superconductor in a magnetic field can be written as

$$G = U - TS - HM \quad (1.2)$$

where M is the magnetization, S is the entropy and the usual pV term is neglected. We may verify Eq. 1.2 by observing that the changes in internal energy density in the presence

of a magnetic field is given by

$$dU = TdS + HdM. \quad (1.3)$$

Then, from Eqs. 1.2 and 1.3, we obtain

$$dG = -SdT - MdH. \quad (1.4)$$

Substituting $M = -H/4\pi$ for a perfect diamagnet ($B = 0$) and integrating Eq. 1.4, we obtain the following important relation for the superconducting state at a given temperature

$$G_s(H) = G_s(0) + \frac{1}{8\pi}H^2. \quad (1.5)$$

From thermodynamic theory we know that for two phases to be in equilibrium (at constant T, P, H), it is necessary that the Gibbs free energies be equal. Thus, along the critical field curve where the superconducting and normal states are in equilibrium,

$$G_n = G_s(0) + \frac{1}{8\pi}H_c^2, \quad (1.6)$$

where G_n is the Gibbs free energy density of the normal state and is essentially independent of the magnetic field. From Eq. 1.4, we obtain

$$\left(\frac{\partial G}{\partial T}\right)_H = -S \quad (1.7)$$

so that Eqs. 1.5 and 1.6 give the important result that in equilibrium

$$S_n - S_s = -\frac{H_c}{4\pi} \frac{dH_c}{dT} \quad (1.8)$$

where S_s denotes the entropy in the superconducting phase in zero field. Since dH_c/dT is always found to be negative, the entropy of the normal state is always greater than that of the superconducting state.

Finally, the difference in heat capacity per unit volume in the superconducting and normal states is given by

$$\Delta C = C_s - C_n = T \frac{d}{dT}(S_s - S_n) = \frac{TH_c}{4\pi} \frac{d^2H_c}{dT^2} + \frac{T}{4\pi} \left[\frac{dH_c}{dT}\right]^2, \quad (1.9)$$

which is shown in Fig. 1.7. At $T = T_c$, where $H_c = 0$, we thus have

$$\Delta C = \frac{T_c}{4\pi} \left(\frac{dH_c}{dT}\right)^2. \quad (1.10)$$

We note from Eq. 1.8 that at the critical temperature $H_c = 0$ so that there is no latent heat of transition ($\Delta S = 0$), but there is, according to Eq. 1.10, a discontinuity in the heat capacity. For this reason the phase transition at $T = T_c$ (where $H_c = 0$) is of second order, but away from T_c , the phase transition has a latent heat and is a first order phase transition.

1.9 Microscopic Description of Superconductivity

From the survey of properties of superconductors outlined in this chapter we see that a description of superconductivity must embody the following features:

- The superconducting state is a special state of the electrons; i.e., it is more than just a perfectly conducting state.
- This special state is quantum mechanical in nature.
- An energy gap exists between the ground state and the states for the excited quasi-particles (electrons).
- The interaction between the electrons and the lattice vibrations is important in the mechanism of conventional superconductivity.

Some of these facts were recognized as early as the late 1930's, but it was not until 1957 that **B**ardeen, **C**ooper, and **S**chrieffer (BCS) developed a microscopic theory of superconductivity and were able to fit all the pieces together. The central result of the BCS theory is that the energy gap is given by

$$E_g = 2\hbar\omega_D \exp\left(-\frac{\lambda_{ep}}{NV}\right) \simeq 3.5k_B T_c \quad (1.11)$$

where ω_D is the Debye phonon frequency, λ_{ep} is a dimensionless coupling constant that describes the strength of the electron-phonon interaction, N denotes the density of single particle states at the Fermi level and V denotes the attractive electron-phonon interaction. Note that T_c and E_g are non-analytic in λ_{ep} which implies that T_c and E_g cannot be expressed in a power series for small λ_{ep} . Therefore, quantum mechanical perturbation theory, the mainstay of theoretical physics, cannot be used to solve the superconductivity problem. What BCS did was to open up a new method in theoretical physics. What they did is exciting, but beyond the scope of this course.

Nevertheless, we will rely on some of the basic BCS results, as will be described in Chapter 2. First, the special state of nearly 10^{23} electrons/cm³ can be described by one quantum mechanical wave function $\Psi(\vec{r})$. Second, the electrons are bound in pairs, the so-called Cooper pairs, which means that electrons with opposite momenta ($+\vec{p}$) and ($-\vec{p}$) and opposite spins (\uparrow) and (\downarrow) are bound by an energy Δ_0 related to the superconducting band gap. Since all the Cooper pairs are the same, we can also think of $\Psi(\vec{r})$ as the wave function for a Cooper pair.

Chapter 2

Macroscopic Quantum Description of Superconductivity

In this chapter, a simple picture of the macroscopic quantum description of superconductivity is presented. The concept of the Cooper pair of electrons with equal and opposite vectors and opposite spins is introduced, along with the wave function for all the electrons in the superconductor. From this macroscopic description of the wavefunction, we derive an expression for the super-current, the London equations for the electro-dynamics, the Meissner effect, perfect conductivity, flux quantization, and the Josephson Effect.

2.1 The Cooper Pair

Most of the distinctive properties of superconductivity are explained by the macroscopic quantum description of superconductivity. The starting point of this description is that all the superconducting electrons, all 10^{23} of them, can be represented quantum mechanically by a single wave function $\Psi(\vec{r})$. Although the exact form of the wave function comes from the Bardeen–Cooper–Schrieffer (BCS) theory, most of the physics of superconductivity follows from the existence of a macroscopic wave function, regardless of the exact form of $\Psi(\vec{r})$.

The physical mechanism for superconductivity lies in a pairing of the Fermi particles to form a Bose gas of paired quasiparticles. The mechanism for this pairing in conventional superconductors is the electron-phonon coupling.

The physical basis for an attraction between two electrons via the electron-phonon interaction was pointed out by Fröhlich in 1950. Suppose that one electron passes through the lattice [see Fig. 2.1(a)]. In so doing, it polarizes the positive ion cores and leaves a lattice distortion in the immediate vicinity of the electron trail. If a second electron enters this region before the lattice relaxes, its energy will be lowered because the lattice is already polarized by the first electron. The mechanism shown in Fig. 2.1(a) thus provides an attractive interaction between the two electrons.

This attractive Fröhlich interaction is represented by the diagram in Fig. 2.1(b) showing an electron of wave vector \vec{k}_1 emitting a phonon of wave vector \vec{q} and being scattered into a state \vec{k}'_1 where $\vec{k}_1 = \vec{k}'_1 + \vec{q}$. Likewise the second electron with wave vector \vec{k}_2 absorbs the phonon so that $\vec{k}_2 + \vec{q} = \vec{k}'_2$ from which it follows that

$$\vec{k}_1 + \vec{k}_2 = \vec{k}'_1 + \vec{k}'_2 = \vec{b} \quad (2.1)$$

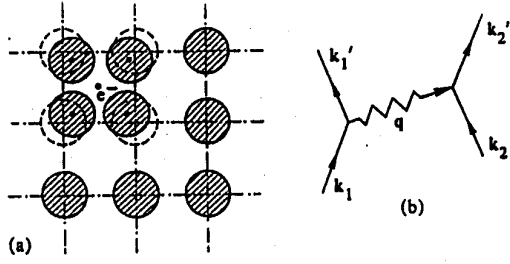


Figure 2.1: (a) A schematic diagram of an electron polarizing positive ions in its vicinity to create an attractive potential for a second electron following in the wake of the first electron. (b) A schematic diagram of an electron–electron interaction transmitted by a phonon of wave vector \vec{q} , such that $\vec{k}_1 + \vec{k}_2 = \vec{k}_1' + \vec{k}_2'$.

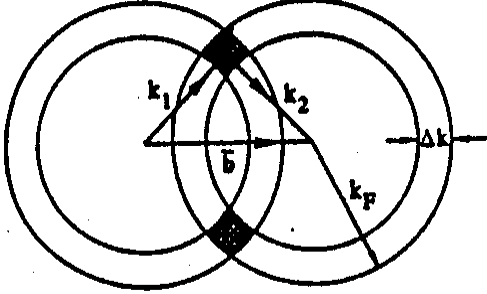


Figure 2.2: Schematic diagram showing two shells in \vec{k} -space of radius k_F and thickness Δk corresponding to the two electrons forming a Cooper pair. The cross-hatched section is a cross section of the ring in which the electrons satisfy the conditions $\Delta k = m\omega_D/(\hbar k_F)$ and $\vec{k}_1 + \vec{k}_2 = \vec{b}$. The volume of this ring has a very sharp maximum when the spheres are concentric and $\vec{k}_1 = -\vec{k}_2$.

which shows the conservation of crystal momentum between the initial and final electron states. The vector \vec{b} denotes the sum of the crystal momenta of this electron pair. If E_1 and E_1' denote the energy of the first electron before and after scattering, respectively, it follows that $\Delta E_1 = |E_1 - E_1'| < \hbar\omega_q$ where $\hbar\omega_q$ is the phonon energy. This argument shows that the energies involved in this attractive interaction are small, since $\omega_q < \omega_D$ (the Debye frequency) and $(\hbar\omega_D/E_F) \sim 10^{-3}$.

The electron–phonon coupling mechanism for superconductivity explains why the highest T_c superconductors are usually metals with the highest resistance in the normal state, since the same mechanism that produces superconductivity (the electron–phonon interaction) also gives rise to carrier scattering in metals in the normal state. The experimental linking of the superconductivity mechanism with the electron–phonon interaction came through the observation of the isotope effect (see §1.7) which showed that for the various mercury isotopes $T_c \propto M^{-1/2}$, where M is the ion mass for each isotope.

Cooper’s seminal contribution to the pairing mechanism was to observe that the energy change implied by the pairing mechanism

$$\Delta E = \frac{\hbar^2}{m} k_F \Delta k \simeq \hbar\omega_D \quad (2.2)$$

also implies

$$\Delta k \simeq \frac{m\omega_D}{\hbar k_F} \quad (2.3)$$

and that the maximum number of electron pairs that would obey Eqs. 2.2 and 2.3 occurs

when $\vec{b} = 0$ or when $\vec{k}_1 = -\vec{k}_2$ (as shown in Fig. 2.2). The Cooper pair is then formed by the electron–phonon interaction between states with wave vectors \vec{k} and $-\vec{k}$ and with opposite spins to maximize the probability that the electrons are close together. The BCS ground state involves the construction of a many body wave function for pairing all the electrons in the Fermi sea to form Cooper pairs with equal and opposite wave vectors and opposite spins. According to BSC theory, the energy of this ensemble of paired states is lowered by $2\Delta \sim 3.5k_B T_c$, the energy gap observed experimentally (see §1.4 and §1.6 of Part IV). From Eq. 2.2, we see that $2\Delta \leq \hbar\omega_D$ corresponds to an estimate of ~ 30 K for the upper limit of T_c for a superconductor for which the pairing mechanism is the electron-phonon interaction. Therefore the discovery in 1987 of a high T_c superconductor with $T_c \sim 100$ K was so surprising.

2.2 Macroscopic Quantum Description of the Supercurrent

Following the discussion in §2.1, the wave function for the superconducting electrons can be represented by a single-valued complex function $\Psi(\vec{r})$, having both a real and imaginary part, and possessing the properties described below. These comments are quite general and are not dependent on the pairing mechanism. Therefore, if the pairing mechanism for high T_c superconductivity is not through the electron–phonon interaction, many of the properties of superconductors enumerated here will still be valid.

We now give a summary of the interpretations of the wave function $\Psi(\vec{r})$:

1. The squared modulus of $\Psi(\vec{r})$ is equal to the density $n_s^*(\vec{r})$ of superconducting Cooper pairs:

$$|\Psi(\vec{r})|^2 = \Psi^*(\vec{r})\Psi(\vec{r}) = n_s^*(\vec{r}) \quad (2.4)$$

The asterisk on the wave function signifies complex conjugation, but the asterisk on n_s^* signifies a convention that n_s^* is the density of Cooper pairs which is half the density of superconducting electrons n_s . That is $2n_s^* = n_s$, since two electrons with wave vectors \vec{k} and $-\vec{k}$ are bound in a Cooper pair. The wavefunction $\Psi(\vec{r})$ thus denotes the degree of superconducting order, and is in that sense an order parameter, which vanishes for $T \geq T_c$ in the normal state.

2. The superconducting current \vec{j}_s is a generalization of the probability current in quantum mechanics

$$\vec{j}_s = \frac{q^*}{2m^*} \left\{ \Psi^* \left(\frac{\hbar}{i} \vec{\nabla} - \frac{q^*}{c} \vec{A} \right) \Psi + \left[\left(\frac{\hbar}{i} \vec{\nabla} - \frac{q^*}{c} \vec{A} \right) \Psi \right]^* \Psi \right\} \quad (2.5)$$

where $q^* = -2|e|$ is the charge on the Cooper pair, $m^* = 2m_0$ is the mass of the Cooper pair, and \vec{A} is the magnetic vector potential, where $\vec{\nabla} \times \vec{A} = \vec{B}$, and m_0 is the free electron mass.

3. The time evolution of the wave function is given by Schrödinger's Equation

$$-\frac{\hbar}{i} \frac{\partial \Psi}{\partial t} = \mathcal{H}\Psi = E\Psi \quad (2.6)$$

where E is the energy for the quantum mechanical state.

2.3 The Quantum Mechanical Current

For completeness, we give here a brief derivation of the quantum mechanical current density \vec{j} for a general potential $V(\vec{r})$. This current density \vec{j} was used to write Eq. 2.5. The derivation relies on the continuity equation

$$\frac{\partial \rho}{\partial t} + \vec{\nabla} \cdot \vec{j} = 0 \quad (2.7)$$

where \vec{j} is the current density, and $\rho(\vec{r}) = qn(\vec{r})$ denotes the charge density. Then we can write

$$\frac{\partial \rho}{\partial t} = q \frac{\partial}{\partial t} n(\vec{r}) = q \frac{\partial}{\partial t} (\Psi \Psi^*) = q \left[\left(\frac{\partial \Psi}{\partial t} \right) \Psi^* + \Psi \left(\frac{\partial \Psi^*}{\partial t} \right) \right]. \quad (2.8)$$

Using the time-dependent Schrödinger equation Eq. 2.6 and its complex conjugate, we obtain

$$\frac{\partial \rho}{\partial t} = q \left[\left(-\frac{i}{\hbar} \right) \Psi^* \mathcal{H} \Psi + \Psi \left(\frac{i}{\hbar} \right) \mathcal{H} \Psi^* \right] \quad (2.9)$$

and substitution of the Hamiltonian

$$\mathcal{H} = \frac{p^2}{2m} + V(\vec{r}) = -\left(\frac{\hbar^2 \vec{\nabla} \cdot \vec{\nabla}}{2m} \right) + V(\vec{r}) \quad (2.10)$$

into Eq. 2.9 consequently yields

$$\frac{\partial \rho}{\partial t} = \left(\frac{q\hbar i}{2m} \right) \left(\Psi^* \vec{\nabla} \cdot \vec{\nabla} \Psi - \Psi \vec{\nabla} \cdot \vec{\nabla} \Psi^* \right) = \vec{\nabla} \cdot \left[\left(\frac{q\hbar i}{2m} \right) (\Psi^* \vec{\nabla} \Psi - \Psi \vec{\nabla} \Psi^*) \right] = -\vec{\nabla} \cdot \vec{j} \quad (2.11)$$

making use of the continuity equation and the fact that since Ψ and Ψ^* only differ by a phase factor, $\vec{\nabla} \Psi$ and $\vec{\nabla} \Psi^*$ commute

$$[\vec{\nabla} \Psi^*, \vec{\nabla} \Psi] = 0. \quad (2.12)$$

We thus identify the current density with

$$\vec{j} = \frac{q}{2m} \left[\Psi^* \left(\frac{\hbar}{i} \vec{\nabla} \right) \Psi - \Psi \left(\frac{\hbar}{i} \vec{\nabla} \right) \Psi^* \right] = \frac{q}{2m} \left[\Psi^* \vec{p} \Psi + \text{c.c.} \right] \quad (2.13)$$

showing that the second term in Eq. 2.13 is the complex conjugate of the first, thereby guaranteeing that \vec{j} is a Hermitian operator that will yield real eigenvalues. In the presence of a magnetic field, we replace \vec{p} by

$$\vec{p} \rightarrow \vec{p} - \frac{q}{c} \vec{A} \quad (2.14)$$

so that Eq. 2.13 then becomes

$$\vec{j} = \left(\frac{q}{2m} \right) \left\{ \Psi^* \left(\frac{\hbar}{i} \vec{\nabla} - \frac{q}{c} \vec{A} \right) \Psi + \left[\Psi^* \left(\frac{\hbar}{i} \vec{\nabla} - \frac{q}{c} \vec{A} \right) \Psi \right]^* \right\} \quad (2.15)$$

where again the second term in Eq. 2.15 is the complex conjugate of the first. If we identify the charge q and the mass m with the effective charge q^* and the effective mass m^* , respectively, then Eq. 2.15 yields Eq. 2.5 for the superconducting current \vec{j}_s .

2.4 The Supercurrent Equation

In considering the role of the wave function $\Psi(\vec{r})$ in the superconductivity problem, the current density given by Eq. 2.15 is a very important and useful equation. Ginzburg and Landau observed that all the Cooper pairs are in the same two-electron state, and therefore a single complex wavefunction can denote the order parameter of the superconducting state. With this interpretation of $\Psi(\vec{r})$ as a complex order parameter for a Cooper pair, then $\Psi(\vec{r})$ can be written in terms of an amplitude and a phase

$$\Psi(\vec{r}) = |\Psi(\vec{r})|e^{i\theta(\vec{r})} = [n_s^*]^{1/2}e^{i\theta(\vec{r})} \quad (2.16)$$

where we have not explicitly considered the time dependence of $\Psi(\vec{r})$. Here we assume that the significant spatial variation of the wave function is through the phase $\theta(\vec{r})$, so that the density of Cooper pairs is essentially independent of position and time. Putting this form of $\Psi(\vec{r})$ into Eq. 2.5 gives:

$$\vec{j}_s = \left(-\frac{q^{*2}n_s^*}{m^*c}\right)\vec{A} + \left(\frac{q^*n_s^*\hbar}{m^*}\right)\vec{\nabla}\theta = \left[-\frac{q^{*2}}{m^*c}\vec{A} + \frac{q^*\hbar}{m^*}\vec{\nabla}\theta\right]|\Psi|^2 \quad (2.17)$$

or

$$\vec{j}_s = -\frac{\vec{A}}{\Lambda_s c} + \frac{\hbar}{q^*\Lambda_s}\vec{\nabla}\theta \quad (2.18)$$

which is the **Supercurrent Equation** in which

$$\frac{1}{\Lambda_s} = \frac{q^{*2}n_s^*}{m^*} = \frac{e^2n_s}{m_0}. \quad (2.19)$$

From Eq. 2.18 we see that the supercurrent \vec{j}_s is driven by two terms. The first term is strictly a classical term which is proportional to the classical vector potential \vec{A} . The second term is a partly quantum mechanical term which is proportional to the gradient of the phase $\theta(\vec{r})$ of the wave function. Although the second term looks purely quantum mechanical, the change of phase can also result from a classical field. For example, if Eq. 2.16 is substituted into the time-dependent Schrödinger equation Eq. 2.6, and if we assume that the amplitude of the wave function is independent of time (which is equivalent to saying that the density of Cooper pairs is time independent), we have simply that

$$\frac{\partial\theta}{\partial t} = -\frac{\mathcal{H}}{\hbar}. \quad (2.20)$$

Therefore, in an applied electrical field, the Hamiltonian is perturbed by the scalar potential $\phi(\vec{r})$

$$\mathcal{H} = \mathcal{H}_0 + q^*\phi(\vec{r}). \quad (2.21)$$

From Eq. 2.20, we see that a classical voltage $q^*\phi(\vec{r})$ causes the quantum mechanical phase of the wavefunction $\theta(\vec{r})$ to change with time.

2.5 The London Equations

We now derive the two London equations which describe the electrodynamics of superconductors from the supercurrent equation (Eq. 2.18). The first London equation relates to the perfect conductivity of superconductors, while the second London equation follows from the perfect diamagnetism condition, or the Meissner effect.

1. Perfect Conductivity - First London Equation

By assuming that the density of Cooper pairs n_s^* is independent of time, then differentiation of Eq. 2.18 yields

$$\frac{\partial \vec{j}_s}{\partial t} = -\left(\frac{1}{c\Lambda_s}\right) \frac{\partial \vec{A}}{\partial t} + \left(\frac{\hbar}{q^*\Lambda_s}\right) \vec{\nabla} \frac{\partial \theta}{\partial t}. \quad (2.22)$$

We can write $(\partial\theta/\partial t)$ in terms of the Hamiltonian from Eq. 2.20 and in the presence of an applied electric field as

$$\hbar \frac{\partial \theta}{\partial t} = -\left(\mathcal{H}_0 + q^*\phi(\vec{r})\right). \quad (2.23)$$

Assuming that \mathcal{H}_0 is independent of position, Eq. 2.22 becomes

$$\frac{\partial \vec{j}_s}{\partial t} = -\Lambda_s^{-1} \left(\frac{\partial \vec{A}}{c\partial t} + \vec{\nabla} \phi\right) = \Lambda_s^{-1} \vec{E}, \quad (2.24)$$

which states that current flows under the influence of an electric field without any damping, $m\vec{v} = e\vec{E}$. This equation relates to the perfect conductivity of superconductors and is known as the first London equation. This equation is usually written as

$$\vec{E} = \Lambda_s \frac{\partial \vec{j}_s}{\partial t} \quad (2.25)$$

where $\Lambda_s = m^*/(q^{*2}n_s^*)$.

2. Perfect Diamagnetism - Second London Equation

By taking the curl of Eq. 2.18, the supercurrent equation, we obtain the second London equation

$$\vec{\nabla} \times \vec{j}_s = -\frac{1}{\Lambda_s c} \vec{B} \quad (2.26)$$

where we note that $\vec{\nabla} \times \vec{\nabla} \theta = 0$ because the curl of a gradient vanishes. Using Maxwell's equation $\vec{\nabla} \times \vec{H} = (4\pi/c)\vec{j}$, neglecting the displacement current, and noting that $\vec{B} = \hat{\mu}\vec{H}$, we obtain

$$\vec{\nabla} \times \vec{\nabla} \times \vec{B} = -\left(\frac{4\pi\hat{\mu}}{c^2\Lambda_s}\right) \vec{B}. \quad (2.27)$$

Since

$$\vec{\nabla} \times \vec{\nabla} \times \vec{B} = \vec{\nabla}(\vec{\nabla} \cdot \vec{B}) - \nabla^2 \vec{B} \quad (2.28)$$

and since $\vec{\nabla} \cdot \vec{B} = 0$, we further obtain

$$\nabla^2 \vec{B} = \frac{1}{\lambda_s^2} \vec{B} \quad (2.29)$$

where λ_s is the superconducting penetration depth and from Eqs. 2.27 and 2.29 we obtain:

$$\lambda_s = \left(\frac{\Lambda_s c^2}{4\pi \hat{\mu}} \right)^{1/2} = \left(\frac{m^* c^2}{4\pi \hat{\mu} q^* n_s^*} \right)^{1/2}. \quad (2.30)$$

The penetration depth λ_s has a magnitude $\lambda_s \sim 1000 \text{ \AA}$, which is obtained by assuming that there are $n_s \sim 10^{23}$ electrons/cm³ and using Eq. 2.19 to yield $\Lambda_s \sim 10^{-31}/\text{sec}^2$. The second London equation thus implies an exponential spatial decay of the B field in the superconductor with a functional dependence

$$B(z) = B(0) \exp(-z/\lambda_s). \quad (2.31)$$

Equation 2.31 is the physical manifestation of the Meissner effect, which states that the \vec{B} field is excluded from the interior of a superconductor. The exponential decay of the \vec{B} field in a superconductor, also leads to the decay of the current density \vec{j}_s in the same superconducting penetration depth. This result is obtained by taking the curl of the second London equation (Eq. 2.26) which gives

$$\vec{\nabla} \times \vec{\nabla} \times \vec{j}_s = -\frac{1}{\Lambda_s c} \vec{\nabla} \times \vec{B} = -\frac{\hat{\mu}}{\Lambda_s c} \vec{\nabla} \times \vec{H} = -\frac{\hat{\mu}}{\Lambda_s c} \left(\frac{4\pi}{c} \right) \vec{j}_s. \quad (2.32)$$

From the continuity equation we can write $\vec{\nabla} \cdot \vec{j} = 0$ for the steady state condition, and we thus obtain a differential equation for \vec{j}_s

$$-\nabla^2 \vec{j}_s = -\left(\frac{\hat{\mu}}{\Lambda_s c} \right) \frac{4\pi}{c} \vec{j}_s = -\left(\frac{1}{\lambda_s^2} \right) \vec{j}_s. \quad (2.33)$$

Thus we see that the second London equation in the steady state leads to an exponential decay of both the \vec{B} field and the supercurrent \vec{j}_s as we move away from the surface into the superconductor. This rapid exponential decay of \vec{B} , \vec{j}_s and also \vec{H} (since $\vec{B} = \hat{\mu} \vec{H}$)

$$B(z) = B(0) e^{-z/\lambda_s} \quad (2.34)$$

$$H(z) = H(0) e^{-z/\lambda_s}. \quad (2.35)$$

$$j_s(z) = j_s(0) e^{-z/\lambda_s} \quad (2.36)$$

clarifies the Meissner effect regarding the exclusion of flux in a superconductor.

2.6 The Two-Fluid Model

The London equations are appropriate at $T = 0$ where all the electrons are in Cooper pairs. To describe the electrodynamics at a finite temperature, a two-fluid model is introduced. According to this model the total current density in a superconductor is considered to be a superposition of the contributions to the current from the superconducting electron pairs and from the normal electrons, which are identified with quasi-electrons that are excited above the superconducting energy gap by breaking Cooper pairs. We then write:

$$j = j_n + j_s \quad (2.37)$$

as the superposition of a normal (resistive) current given by

$$\vec{j}_n = \sigma \vec{E} \quad (2.38)$$

and a superconducting current \vec{j}_s . Then from Maxwell's equations, we can write

$$\left(\frac{c}{\hat{\mu}}\right) \vec{\nabla} \times \vec{B} = 4\pi(\sigma \vec{E} + \vec{j}_s) + \epsilon \dot{\vec{E}}, \quad (2.39)$$

in which we have also included the displacement current $\dot{\vec{D}} = \epsilon \dot{\vec{E}}$. We can thus write

$$\left(\frac{c}{\hat{\mu}}\right) \vec{\nabla} \times \vec{\nabla} \times \vec{B} = -\left(\frac{c}{\hat{\mu}}\right) \vec{\nabla}^2 \vec{B} = 4\pi(\sigma \vec{\nabla} \times \vec{E} + \vec{\nabla} \times \vec{j}_s) + \epsilon \vec{\nabla} \times \dot{\vec{E}}, \quad (2.40)$$

or, using Eq. 2.26 for $\vec{\nabla} \times \vec{j}_s$, we obtain

$$\frac{1}{\hat{\mu}} \nabla^2 \vec{B} = \frac{4\pi\sigma}{c^2} \dot{\vec{B}} + \frac{4\pi}{\Lambda_s c^2} \vec{B} + \epsilon \frac{\ddot{\vec{B}}}{c^2}. \quad (2.41)$$

If we seek a plane wave solution

$$B \sim \exp[-i(\omega t - \vec{k} \cdot \vec{r})], \quad (2.42)$$

then Eq. 2.41 gives

$$\frac{k^2 c^2}{\hat{\mu}} = -\frac{4\pi}{\Lambda_s} + 4\pi\sigma\omega i + \epsilon\omega^2. \quad (2.43)$$

The successive terms on the right hand side of Eq. 2.43 represent the effects of the superconducting penetration depth, the ordinary eddy current skin depth, and the displacement current. Equation 2.43 determines the propagation characteristics at finite temperature of a superconductor in an electromagnetic field.

In the limit of low frequencies,

$$k \cong i \left(\frac{4\pi\hat{\mu}}{\Lambda_s c^2} \right)^{\frac{1}{2}}, \quad (2.44)$$

which represents the exponential decay of the B field discussed in §2.5, where the superconducting penetration depth λ_s is given by

$$\lambda_s = \left(\frac{\Lambda_s c^2}{4\pi\hat{\mu}} \right)^{\frac{1}{2}} = \left(\frac{mc^2}{4\pi n e^2 \hat{\mu}} \right)^{\frac{1}{2}}, \quad (2.45)$$

and λ_s is one of the important length scales in a superconductor. Here m , n and e refer to single electron states, utilizing the relation between the characteristics of Cooper pairs and the single electron states (see Eq. 2.19).

We recall that for a **normal** conductor in a time-varying ac magnetic field, that the magnetic field is confined to a skin depth near the surface of thickness $\delta_n = c(2\pi\hat{\mu}\omega\sigma)^{-1/2}$. In the radio frequency range, $\delta_n \gg \lambda_s$, so that the superconducting decay length dominates the spatial variations of the magnetic field. In the millimeter wave range δ_n and λ_s can be of comparable magnitudes, but then for most conventional superconductors the electromagnetic frequency would exceed the superconducting band gap, and would serve to break the Cooper pairs and give rise to behavior similar to that observed in a normal metal.

2.7 Flux Quantization

Besides perfect conductivity and perfect diamagnetism (Meissner effect), quantization of the magnetic flux is characteristic of superconductivity. Flux quantization follows directly from Eq. 2.18, the supercurrent equation, and from the interpretation of the wave function, as discussed below. Rearranging Eq. 2.18, we have

$$\vec{\nabla}\theta = q^* \left(\frac{\Lambda_s}{\hbar} \right) \vec{j}_s + \left(\frac{q^*}{\hbar c} \right) \vec{A}. \quad (2.46)$$

Integrating Eq. 2.46 around a closed contour yields the phase difference around the contour

$$\oint_c \vec{\nabla}\theta \cdot d\vec{s} = q^* \frac{\Lambda_s}{\hbar} \oint_c \vec{j}_s \cdot d\vec{s} + \frac{q^*}{\hbar c} \oint_c \vec{A} \cdot d\vec{s}. \quad (2.47)$$

Now, the first term on the left of Eq. 2.47 can be integrated directly to yield a phase difference

$$\oint_c (\vec{\nabla}\theta) \cdot d\vec{s} = \theta_2 - \theta_1 \quad (2.48)$$

where $\theta_2 - \theta_1$ is the phase difference of the wave function in going around a closed loop. Our interpretation of the complex wave function, $|\Psi(\vec{r})|e^{i\theta}$, where $|\Psi(\vec{r})|^2$ equals the density of Cooper pairs, $|\Psi(\vec{r})|^2 = n_s^*$, demands only that the modulus be a single-valued function. The phase can in general be multi-valued as long as the function $\Psi(\vec{r})$ is invariant under rotation by 2π or in other words $e^{i(\theta_1 - \theta_2)} = 1$. From this argument it follows that $\theta_1 - \theta_2 = \pm 2\pi n$.

The last term in Eq. 2.47 becomes, after using Stokes' theorem,

$$\oint_c \vec{A} \cdot d\vec{s} = \int_s (\vec{\nabla} \times \vec{A}) \cdot d\vec{S} = \int_s \vec{B} \cdot d\vec{S} = \Phi \quad (2.49)$$

where Φ is the flux enclosed by the contour and S is the area defined by the contour. Hence, Eq. 2.47 becomes

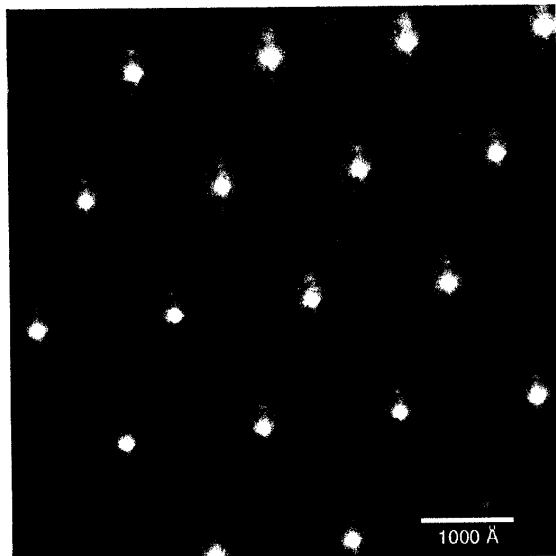
$$\pm 2\pi n = \frac{q^* \Lambda_s}{\hbar} \oint_c \vec{j}_s \cdot d\vec{s} + \frac{q^*}{\hbar c} \Phi \quad (2.50)$$

where n is an integer. If the path of the line integral for the supercurrent is chosen to be deep inside the superconducting material, so that $\vec{j}_s = 0$, then

$$|\Phi| = \frac{\hbar c}{q^*} 2\pi n = \frac{\hbar c}{q^*} n \quad (2.51)$$

which gives the quantization of flux in units of $(\hbar c/q^*) = \Phi_0$, if the supercurrent flows around the path of the superconductor. For $|q^*| = |2e|$ we thus obtain a magnitude for the flux quantum $\Phi_0 = \hbar c/2e = 2.07 \times 10^{-7} \text{gauss cm}^2 = 2.07 \times 10^{-15} \text{tesla m}^2$. As an example of flux quantization, consider the metallic torus (see Fig. 1.2) which is cooled in a magnetic field to a temperature below T_c . If the magnetic field is then removed, flux will be trapped. Suppose that a is the radius of the cross section of the torus. Then if $a \gg \lambda_s$, then all the currents decay exponentially from the surface of the torus. By considering a contour many penetration depths from the surface, the current density j_s can be made negligibly small. Hence, the quantization condition of Eq. 2.51 states that the flux Φ passing through the torus is quantized in units of Φ_0 or that $\Phi = n\Phi_0$.

Figure 2.3: Triangular lattice of flux lines through the top surface of a superconducting cylinder as observed in an electron microscope. The points where the flux lines exit the surface are decorated with fine ferromagnetic particles.



2.8 The Vortex Phase and Trapped Flux

Physically, the lower critical field H_{c1} (see Fig. 1.6) denotes an applied magnetic field large enough to create one fluxoid in the area of flux penetration (estimated as $\pi\lambda_s^2$)

$$\pi\lambda_s^2\hat{\mu}H_{c1} = \Phi_0 \quad (2.52)$$

where λ_s is the superconducting penetration depth. Thus, H_{c1} measures the initiation of flux penetration into a type II superconductor.

In the vortex state of a type-II superconductor, the vortices form a regular lattice (see Fig. 2.3). This can be understood physically if we recognize that two vortices of the same sign repel one another which maximizes their distance apart, while requiring a fixed number density to account for the specified flux penetration. There are many examples in physics of ordering caused by similar competing processes. For simplicity, we consider the vortex lattice to be a square array, although the results given below are independent of the type of regular array (i.e., whether it is triangular or square). Consider an infinite slab of a vortex array (such as in Fig. 2.3) with the field perpendicular to the top surface. Suppose that the vortices are a distance $2a$ apart and have a non-superconducting (normal) core of radius ξ_s which is surrounded by superconducting material.

Consider the contour c for the line integral in Eq. 2.50 drawn along the perpendicular bisectors between one vortex and its nearest neighbor vortices. If flux goes through each vortex, there must be a circulating current around each vortex. By symmetry, the circulating currents are identically zero along a contour drawn along the bisectors of the distance between the vortices. (A similar contour with $\vec{j}_s = 0$ can be found for any regular array). Hence, the quantization condition (Eq. 2.51) requires the flux within the contour to be an integral number of flux quanta $n\Phi_0$. The same condition holds for each vortex, so that for a triangular lattice $n\Phi_0 = \hat{\mu}H_a(3\sqrt{3}/2)a^2$, where H_a is the applied magnetic field.

Experimentally, $n = 1$ for type II superconductors at the closest packing of the vortices. Hence, $H_{c2} = \Phi_0/[\hat{\mu}\xi_s^2(3\sqrt{3}/2)]$ for the closest packing of the vortices, which we explain as follows. As the applied field is increased above H_{c1} , the spacing $2a$ between vortices becomes smaller and smaller. The spacing can only get as small as some minimal distance $a = \xi_s$, when the cores on adjacent vortices begin to overlap and the material becomes normal. This minimal distance ξ_s is called the superconducting coherence distance, and is an important length scale in a superconductor. The externally applied field corresponding to $a = \xi_s$ is called the “upper critical field” H_{c2} , so that $H_{c2} = \Phi_0/(\hat{\mu}3\sqrt{3}\xi_s^2/2)$.

Since the magnetic field will be uniform within the core, the field, and hence also the currents, will fall off exponentially from the edge of the core as long as $a \gg \lambda_s$. For most type-II superconductors $\lambda_s \gg \xi_s$, so that most of the flux is contained in an area λ_s^2 around the core, and a very small fraction of the flux $(\xi_s^2/\lambda_s^2)\Phi_0 \ll \Phi_0$ is in the core itself. Therefore, by considering a contour very near the edge of the core, the quantization condition gives

$$\Phi_0 = \frac{4\pi\hat{\mu}\lambda_s^2}{c} \oint \vec{j}_s \cdot d\vec{s} + \frac{\xi_s^2}{\lambda_s^2} \Phi_0 \quad (2.53)$$

and neglecting the term in $(\xi_s^2/\lambda_s^2)\Phi_0$ we can write

$$\Phi_0 = \frac{4\pi\hat{\mu}\lambda_s^2}{c} \oint \vec{j}_s \cdot d\vec{s}. \quad (2.54)$$

That is, near the core it is the line integral of the current which is quantized in integral numbers of flux units. The circulating current near the core is in the \vec{i}_ϕ circumferential direction. Carrying out the line integral in Eq. 2.54 thus yields

$$\Phi_0 = \frac{4\pi\hat{\mu}\lambda_s^2}{c} j_s 2\pi r \quad (2.55)$$

or

$$j_s = \frac{\Phi_0 c}{2(2\pi)^2 \hat{\mu} \lambda_s^2} \frac{1}{r}. \quad (2.56)$$

Thus for a vortex we see that the current density decreases as $1/r$, which is also true for a hydrodynamic vortex (e.g., water flowing down a drain). By noting that

$$\vec{j}_s = n_s^* q^* \vec{v}_s \quad (2.57)$$

and writing

$$\frac{4\pi\hat{\mu}\lambda_s^2}{c^2} = \Lambda_s = \frac{m^*}{n_s^* q^{*2}} \quad (2.58)$$

we have,

$$j_s = n_s^* q^* v_s = \frac{c^2 h / (2e)}{2\pi c^2 (m^* / n_s^* q^{*2})} \frac{1}{r} = \frac{\hbar n_s^* q^{*2}}{m^*} \frac{1}{r} \quad (2.59)$$

or

$$v_s = \frac{\hbar}{m^*} \frac{1}{r} \quad (2.60)$$

yielding the quantization condition

$$\int \vec{v}_s \cdot d\vec{l} = \frac{h}{m^*}. \quad (2.61)$$

Furthermore, the velocity cannot be made arbitrarily large, because the minimum size of r is the superconducting coherence distance $r \geq \xi_s$, the coherence distance, thus yielding

$$v_{max} = \frac{\hbar}{m^*} \frac{1}{\xi_s}. \quad (2.62)$$

The circulating currents acquire an additional kinetic energy in circulating around the vortices. However, if this additional kinetic energy exceeds Δ_0 , where $2\Delta_0$ is the gap energy, the Cooper pairs will unbind. That is why the core region of a vortex cannot be superconducting but must be normal! To estimate the core size, note that

$$\Delta_0 = \delta \left(\frac{1}{2} m^* v^2 \right) = m^* v \delta v. \quad (2.63)$$

Since the electrons forming the Cooper pairs are at the Fermi surface, we can write $v = v_F$ and $\delta v = v_s$, where v_s is the velocity of the Cooper pair. Therefore, using Eq. 2.62 and writing δv_s as the maximum vortex velocity we obtain:

$$\Delta_0 \approx m^* v_F \left(\frac{\hbar}{m^*} \frac{1}{\xi_s} \right) \quad (2.64)$$

so that

$$\xi_s \approx \frac{\hbar v_F}{\Delta_0}. \quad (2.65)$$

From the BCS theory of superconductivity, ξ_s for a clean material with very little scattering is given by

$$\xi_0 = \frac{\hbar v_F}{\pi \Delta_0} \quad (2.66)$$

where ξ_0 is called the “**BCS coherence length**”, and is the length over which Cooper pairs are correlated in the absence of any scattering.

2.9 Summary of Length Scales

We list in Table 2.1 some of the characteristic lengths found in superconductors. In §2.5, we discussed the superconducting penetration depth λ_s

$$\lambda_s = \left(\frac{m_0 c^2}{4\pi n \hat{\mu} e^2} \right)^{1/2} \quad (2.67)$$

which governs the penetration of magnetic fields and supercurrents in the superconducting state (see Eqs. 2.34 – 2.36). In most cases, the superconducting penetration depth is much smaller than the penetration depth for metals in the normal state δ_n

$$\delta_n = \frac{c}{(2\pi \hat{\mu} \omega \sigma)^{1/2}}. \quad (2.68)$$

Important parameters for type II superconductors are the intrinsic superconducting coherence length ξ_0 which by the BCS theory is written as

$$\xi_0 = \frac{\hbar v_F}{\pi \Delta_0} \quad (2.69)$$

Table 2.1: Some characteristic length scales for superconducting materials. The superconductors with $\kappa = \lambda_s^0/\xi_0 > 1/\sqrt{2} = 0.71$ are type II. Here λ_s^0 and ξ_0 are the superconducting penetration depth and coherence length in the clean limit.

| Material | $\lambda_s^0(\text{\AA})$ | $\xi_0(\text{\AA})$ | λ_s^0/ξ_0 |
|---|---------------------------|---------------------|---------------------|
| Sn | 3,400 | 23,000 | 0.16 |
| Al | 1,600 | 160,000 | 0.01 |
| Pb | 3,700 | 8,300 | 0.45 |
| Cd | 11,000 | 76,000 | 0.14 |
| Nb | 3,900 | 3,800 | 1.02 |
| YBa ₂ Cu ₃ O _{7-x} | 170 | 3.0 | 56 |
| YBa ₂ Cu ₃ O _{7-x} ⊥ | 6,400 | 16.4 | 390 |

and the coherence length ξ_s in real superconducting materials (in the dirty limit) is given by

$$\xi_s = (\xi_0 \ell_n)^{1/2} \quad (2.70)$$

where ℓ_n is the mean free path for the carriers in the normal state, and is temperature dependent. Likewise, the superconducting penetration depth λ_s in dirty superconductors (i.e., $\ell_n \ll \xi_0$) is given by

$$\lambda_s = \lambda_s^0 \left(\frac{\xi_0}{\ell_n} \right)^{1/2} \quad (2.71)$$

where λ_s^0 is the superconducting penetration depth (see Table 2.1) for large ℓ_n (e.g., $\ell_n > \xi_0$). From Eqs. 2.70 and 2.71, we then conclude that

$$\kappa \equiv \frac{\lambda_s}{\xi_s} = \frac{\lambda_s^0}{\ell_n}. \quad (2.72)$$

The parameter κ defined by Eq. 2.72 is used to distinguish type I superconductors ($\kappa < 1/\sqrt{2}$) from type II superconductors ($\kappa > 1/\sqrt{2}$), and typical values of κ for some superconductors are given in Table 2.1. Thus the decrease in ℓ_n favors type II superconductivity (see Fig. 2.4), but in the limit of small ℓ_n we have $\xi_s \ll \xi_0$ with a relatively low ξ_s . One major contrast between conventional superconductors and high T_c superconductors is the relatively high κ values for the high T_c superconductors.

2.10 Weakly-Coupled Superconductors – The Josephson Effect

Suppose that a thin nominally non-superconducting region connects two superconductors (see Fig. 2.5). Then the wavefunctions of the Cooper pairs in the two superconductors can overlap and produce a coupling between them. Put another way, we can say that the two regions of strong superconductivity are now connected by a region of weak superconductivity or by a weak link. It also seems plausible that the detailed properties of the non-superconducting region won't matter too much other than to establish the thickness required to get appreciable coupling between the superconductors.

Figure 2.4: Penetration depth λ_s and the coherence length ξ as functions of the mean free path l_n of the conduction electrons in the normal state. All lengths are in units of ξ_0 , the intrinsic coherence length. The curves are sketched for $\xi_0 = 10\lambda_s^0$, where λ_s^0 is the superconducting penetration depth for large l_n . For short mean free paths the coherence length becomes shorter and the penetration depth becomes longer. A decrease in l_n favors type II superconductivity.

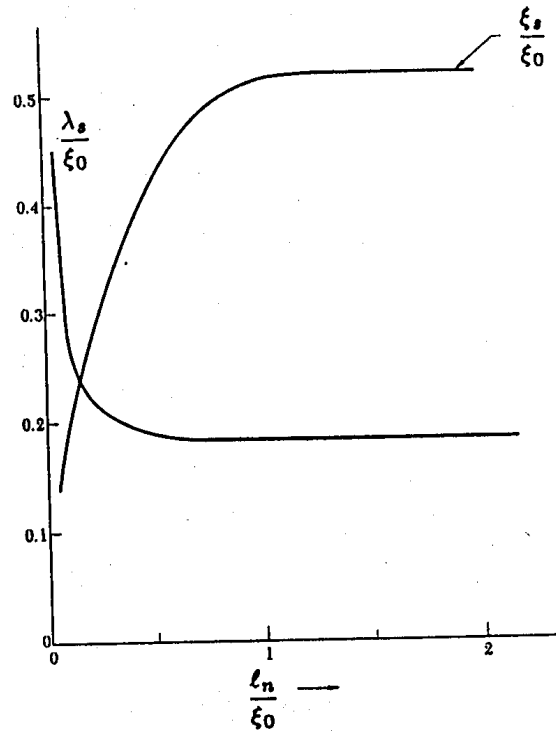
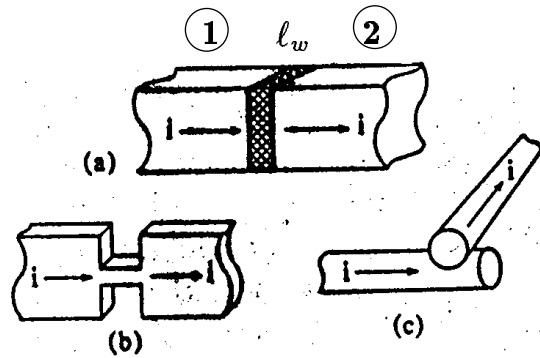


Figure 2.5: Schematic diagram for (a) a Josephson junction. (b) and (c) are schematic diagrams for various kinds of weak links. All of these cases exhibit the Josephson effect.



Assume that at the two boundaries of the weak link region we set the wave functions across the boundaries equal to one another (see Fig. 2.5). Then, if we make the reasonable assumption that in general $\Psi(\vec{r})$ decays exponentially from the edges, we have to a first approximation (valid if $\ell_w \gg \xi_N$, where ξ_N is the characteristic decay length of the Cooper pair wave function in the junction region and ℓ_w is the length of the weak link). Thus we write for the wave function in the weak link (normal state)

$$\Psi_N(x) = |\Psi_{N1}|e^{-x/\xi_N} + |\Psi_{N2}|e^{-(\ell_w-x)/\xi_N}e^{i\Delta\theta} \quad (2.73)$$

where the factor $e^{i\Delta\theta}$ accounts for the very important fact that the phase of the wave function for the Cooper pair on the two sides of the weak link will not in general be the same.

More generally, we could assume that $\Psi_N(x)$ is governed by the equation

$$\xi_N^2 \frac{d^2 \Psi_N(x)}{dx^2} = \Psi_N(x) \quad (2.74)$$

subject to the boundary conditions $\Psi_N(0) = \Psi_{N1}$ and $\Psi_N(\ell) = \Psi_{N2}$. In this case $\Psi_N(x)$ can be written in the form

$$\Psi_N(x) = f_1(x) + f_2(\ell_w - x)e^{i\Delta\theta} \quad (2.75)$$

where $f_1(x)$ and $f_2(x)$ are governed by an equation of the form

$$\xi_N^2 \frac{d^2 f}{dx^2} = f \quad (2.76)$$

with the boundary conditions

$$f_{1,2}(0) = |\Psi_{N1,N2}|. \quad (2.77)$$

Neglecting the presence of magnetic fields for the moment, the current through the junction can be calculated using Eq. 2.13, and we obtain the result

$$\vec{j}_s = \frac{q^* \hbar}{2m^* i} \left(\Psi^* \vec{\nabla} \Psi - \Psi \vec{\nabla} \Psi^* \right) = \frac{q^* \hbar}{m^*} \text{Im}(\Psi^* \vec{\nabla} \Psi) \quad (2.78)$$

and using Eq. 2.73 for Ψ we obtain

$$j_s = \frac{2q^* \hbar}{m^* \xi_N} |\Psi_{N1}| |\Psi_{N2}| \sin \Delta\theta \quad (2.79)$$

which we write as

$$j_s = j_0 \sin \Delta\theta \quad (2.80)$$

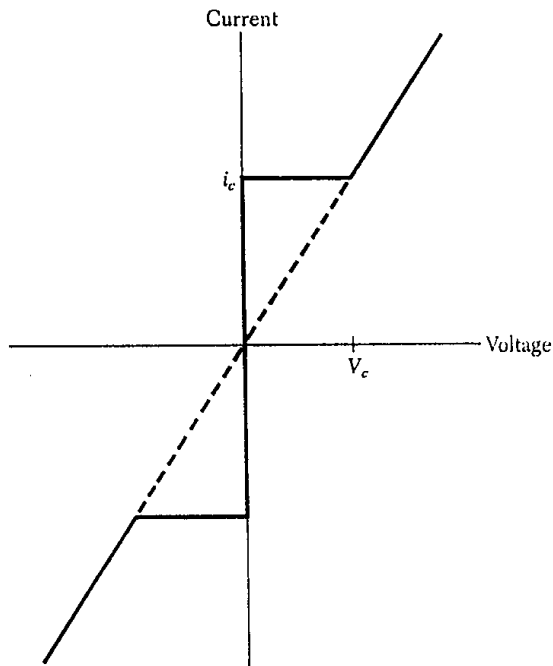
where

$$j_0 = \frac{2q^* \hbar}{m^* \xi_N} |\Psi_{N1}| |\Psi_{N2}| \quad (2.81)$$

and $\Delta\theta$ is the phase difference of the superconducting wave function across the weak link.

Equation 2.80 states that dc tunneling of Cooper pairs can occur when the current density is less than the maximum value j_0 . For current density values above j_0 , some of the current must be carried by normal electrons, and there must be a voltage drop across the

Figure 2.6: Current-voltage characteristics of a Josephson junction. Dc currents flow under zero applied voltage up to a critical current i_c (or critical current density j_0); this is the dc Josephson effect. At voltages above V_c the junction has a finite resistance. Below V_c the current has an oscillatory component of frequency $\omega_J = 2eV/\hbar$: this is the ac Josephson effect.



junction. We thus interpret j_0 as the maximum current that can pass through a Josephson junction before driving it normal (see Fig. 2.6).

We thus obtain the remarkable result that the current is a sinusoidal function of the phase difference across the superconductor. Such behavior is known as the dc Josephson effect. Although Josephson first predicted this result from the point of view of tunneling through an oxide barrier between two superconductors, it is a quite general property of weakly coupled superconductors as our discussion above suggests. Josephson recognized this fact also and was one for the first to emphasize the generality of the Josephson effect. For his extremely important discovery, Josephson was awarded the Nobel Prize in 1973.

Referring to Eqs. 2.20 and 2.21 we see that the time derivative of the phase difference across a Josephson junction is given by

$$\frac{\partial}{\partial t}(\theta_2 - \theta_1) = -\frac{2eV}{\hbar} \quad (2.82)$$

so that

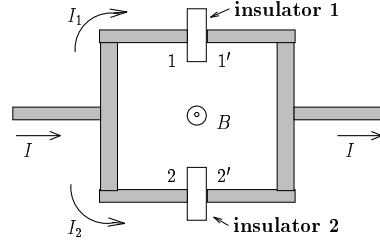
$$\theta_2 - \theta_1 = -\frac{2eV}{\hbar} t \quad (2.83)$$

which states that the current in Eq. 2.80 oscillates with a frequency

$$\omega_J = \frac{2eV}{\hbar}. \quad (2.84)$$

This time dependent oscillation is known as the ac Josephson effect. A dc voltage of 1 μV across the Josephson junction produces a phase oscillation frequency ω_J of 483.6 MHz. Equation 2.84 implies that when a Cooper pair crosses the weak link junction a photon of frequency ω_J is emitted or absorbed.

Figure 2.7: The geometrical arrangement demonstrating macroscopic superconducting quantum interference in a SQUID. A magnetic flux Φ passes through the interior of the loop containing two Josephson junctions.



2.11 Effect of Magnetic Fields on Josephson Junctions – Superconducting Quantum Interference

The fact that the current through a Josephson junction depends on the quantum phase difference across the junction gives rise to quantum interference effects in circuits containing these junctions. Moreover, from the supercurrent equation (Eq. 2.18) we see that the phase differences introduced by the Josephson junction will be sensitive to the presence of magnetic fields. These quantum interference effects are a spectacular demonstration of the quantum nature of superconductivity. The Josephson effect is also important from a practical point of view, because of the great sensitivity of circuits containing Josephson junctions to magnetic fields, making possible very sensitive magnetometers using these quantum interference effects. These devices are called SQUID's (superconducting quantum interference devices). At the same time the magnetic field provides a way of altering the electrical characteristics of single Josephson junctions, thereby providing a way to convert these junctions into three-terminal devices. As is well known, three-terminal devices are much more versatile than two-terminal devices in electronic circuitry.

2.12 Quantum Interference Between Two Junctions

Consider a parallel-connected superconducting circuit in which each arm of the circuit contains a Josephson junction denoted as an insulator in Fig. 2.7. Assume for the moment that the junction behaves uniformly so that the phase change across the junction is the same over the entire junction. The total current flowing through the two junctions connected in parallel is then written as

$$I = I_1 + I_2 = I_{01} \sin \Delta\theta_1 + I_{02} \sin \Delta\theta_2 \quad (2.85)$$

where I_{01} and I_{02} are the current amplitudes through the individual junctions, while $\Delta\theta_1$ and $\Delta\theta_2$ are the phase differences across each of the junctions.

Clearly, the total current I that can be passed through the two junctions depends on $\Delta\theta_1 - \Delta\theta_2$. When $\Delta\theta_1 = \Delta\theta_2$, the currents in the individual arms add, but when $\Delta\theta_1 - \Delta\theta_2 = \pi$, they cancel. In a quantum interference device a magnetic field is used to vary the flux through the current loop, as shown in Fig. 2.7, so that the phase difference $\Delta\theta_1 - \Delta\theta_2$ can be varied by any desired amount of flux Φ enclosed within the circuit. This magnetic flux can be found by taking the line integral of the supercurrent equation (Eq. 2.18)

and imposing the requirement that the wavefunction be single valued after completing a 2π excursion around the circuit.

More explicitly, from the single valuedness requirement, we have

$$\oint_c \vec{\nabla}\theta \cdot d\vec{\ell} = 2\pi n. \quad (2.86)$$

Then using the relation Eq. 2.18 we obtain an expression for the gradient of the phase of the superconducting wave function in a magnetic field

$$\vec{\nabla}\theta = \left(\frac{m^*}{\hbar}\right)\vec{v}_s + \left(\frac{q^*}{c\hbar}\right)\vec{A} \quad (2.87)$$

in the bulk superconductors connecting the junctions. Then applying Eq. 2.87 to 2.86 and noting the direction of current flow we obtain

$$\left(\Delta\theta_1 - \Delta\phi_2\right) + \frac{q^*}{c\hbar} \oint \vec{A} \cdot d\vec{\ell} = 2\pi n \quad (2.88)$$

where we have taken the contour c in Eq. 2.86 deep enough in the superconductor so that $v_s = 0$ along c (except of course in the junctions themselves). We thus obtain

$$\Delta\theta_1 - \Delta\theta_2 + 2\pi\frac{\Phi}{\Phi_0} = 2\pi n \quad (2.89)$$

where we have expressed the magnetic flux within the current loop in units of the flux quantum $\Phi_0 = ch/2e$.

Equation 2.89 shows that the phase difference $\Delta\theta_1 - \Delta\theta_2$ between the two junctions is solely determined by the flux enclosed within the circuit. The flux Φ depends on both the applied field present and also upon any fields produced by the currents circulating in the circuit itself. Since the maximum possible circulating current around the circuit is I_0 , the flux produced by I will be negligible (i.e., there will be no self-shielding) if $I_0L \ll \Phi_0$, where L is the loop inductance on the circuit. In the case where the loop inductance can be neglected, we have the result $\Phi = \Phi_a$, where Φ_a is the applied flux.

Suppose that the two Josephson junctions in Fig. 2.7 are identical and have a phase difference $\Delta\theta = \Delta\theta_1 = \Delta\theta_2$ in zero magnetic field. In a magnetic field the phase difference across each Josephson junction then becomes $\Delta\theta_1 + \pi\frac{\Phi}{\Phi_0}$ and $\Delta\theta_2 - \pi\frac{\Phi}{\Phi_0}$. Then using Eq. 2.80 for the Josephson current and assuming the two junctions in Fig. 2.7 to be identical, we obtain

$$\begin{aligned} I &= I_{01} \sin\left(\Delta\theta + \frac{\pi\Phi}{\Phi_0}\right) + I_{02} \sin\left(\Delta\theta - \frac{\pi\Phi}{\Phi_0}\right) \\ &= I_0 \left[\left(\sin\Delta\theta \cos\pi\Phi/\Phi_0 + \sin\pi\Phi/\Phi_0 \cos\Delta\theta \right) + \left(\sin\Delta\theta \cos\pi\Phi/\Phi_0 - \sin\pi\Phi/\Phi_0 \cos\Delta\theta \right) \right] \\ &= 2I_0 \sin\Delta\theta \cos\pi\Phi/\Phi_0 \end{aligned} \quad (2.90)$$

where $I_0 = I_{01} = I_{02}$ and $\Delta\theta = \Delta\theta_1 = \Delta\theta_2$. Equation 2.90 shows that the parallel combination of junctions in a magnetic field acts very much like a single junction in zero field that is now modulated by the magnetic flux passing through the current loop. Thus Eq. 2.90 has a periodicity shown in Fig. 2.8 with maxima occurring whenever

$$\frac{e\Phi}{\hbar c} = s\pi \quad (2.91)$$

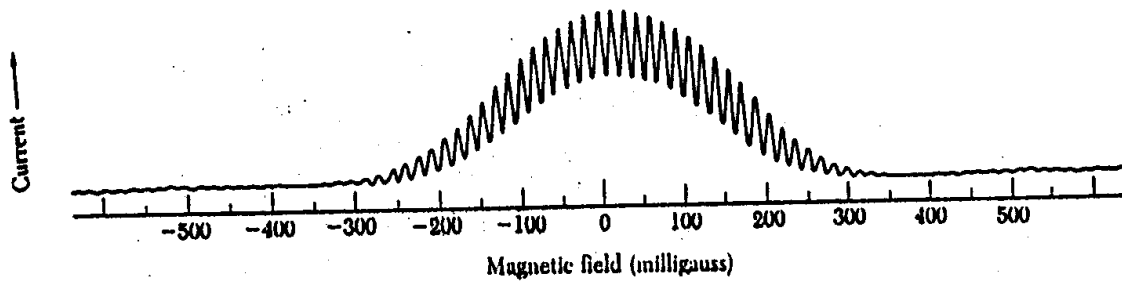


Figure 2.8: Josephson interference from two parallel junctions such as in Fig. 2.7. Josephson interference is mathematically identical to a two-slit interferogram.

where s is an integer. The resulting interference pattern is shown in Fig. 2.8. The short period variation is produced by the interference condition between the two junctions as predicted by Eq. 2.91, and the longer period variation is a diffraction effect arising from the finite dimensions of each junction.

The interference pattern in Fig. 2.8 is formally analogous to a two-slit interference pattern in physical optics. In the case of the SQUID device the “phase difference” is determined by the flux enclosed in the ring. Since a very small amount of flux can be detected in this way (a small fraction of the unit of quantum flux $\Phi_0 = 2.07 \times 10^{-7} \text{gauss cm}^2$), SQUID’s can be used as very sensitive magnetometers. Large arrays of Josephson junctions have also been used to model 2D phase transitions in magnetic systems, and SQUID magnetometers have become the standard equipment for magnetic susceptibility measurements.

Chapter 3

Microscopic Quantum Description of Superconductivity

3.1 Bardeen-Cooper-Schrieffer (BCS) Theory

3.1.1 The Cooper Instability

References:

- L. N. Cooper, “Bound Electron Pairs in a Degenerate Fermi Gas,” *Phys. Rev.* **104**, 1189 (1956).
- J. Bardeen, L. N. Cooper, and J. R. Schrieffer, “Theory of Superconductivity,” *Phys. Rev.* **108**, 1175 (1957).
- T. van Duzer and C.W. Turner, *Principles of Superconductive Devices and Circuits*, Elsevier, NY (1981).

Cooper’s 1956 paper demonstrated that the energy of a Fermi system can be lowered by the formation of weakly bound electron pairs at $T = 0$ for any attractive interaction, no matter how small. This landmark paper paved the way for the full-blown BCS theory, which was published shortly afterward. Here we will show the derivation of the famous BCS formula for T_c as given in Cooper’s paper, which contains many of the important ideas of the BCS paper.

Let us therefore follow Cooper’s derivation. Consider an arbitrarily weak interaction between electrons, \mathcal{H}_1 . If the interaction is small, then there is a minimum energy $\epsilon_{\min} = (\hbar^2 q_{\min}^2)/2m$ below which its effect will be so small that it can approximately be ignored. Likewise there should also be a maximum energy, $\epsilon_{\max} = (\hbar^2 q_{\max}^2)/2m$. Since we know that in real superconductors the electron–electron interaction is phonon–mediated, we can assume that the minimum energy for which the perturbation \mathcal{H}_1 is non–negligible is about $(E_F - \hbar\omega_D)$, and the maximum energy is about $(E_F + \hbar\omega_D)$ where ω_D is the Debye frequency, so that $\epsilon_{\max} - \epsilon_{\min} = 2\hbar\omega_D$.

For the wavefunctions of the assumed electron pairs, we can take the simplest possible form,

$$\phi(\vec{k}_1, \vec{k}_2; \vec{r}_1, \vec{r}_2) = \frac{1}{V} e^{i(\vec{k}_1 \cdot \vec{r}_1 + \vec{k}_2 \cdot \vec{r}_2)} \quad (3.1)$$

where the spins of the two electrons in question must be antiparallel, so that their overall wavefunction will be antisymmetric under interchange of their coordinates, as is required for Fermions. If we now let

$$\begin{aligned}\vec{R} &= \frac{1}{2}(\vec{r}_1 + \vec{r}_2), \\ \vec{r} &= (\vec{r}_2 - \vec{r}_1), \\ \vec{K} &= (\vec{k}_1 + \vec{k}_2), \quad \text{and} \\ \vec{k} &= \frac{1}{2}(\vec{k}_2 - \vec{k}_1)\end{aligned}\tag{3.2}$$

in order to change to center of mass coordinates, then

$$\phi(\vec{k}_1, \vec{k}_2; \vec{r}_1, \vec{r}_2) = \frac{1}{V} e^{i(\vec{K}\cdot\vec{R} + \vec{k}\cdot\vec{r})},\tag{3.3}$$

and the energy becomes

$$E = \frac{\hbar^2}{2m}(k_1^2 + k_2^2) = \frac{\hbar^2}{m}\left(\frac{K^2}{4} + k^2\right) = \epsilon_K + \epsilon_k\tag{3.4}$$

We can equally well write the Cooper pair wave function as

$$\Psi_{\vec{K}}(\vec{R}, \vec{r}) = \frac{1}{V} e^{i(\vec{K}\cdot\vec{R})} \sum_{\vec{k}} a_{\vec{k}} e^{i\vec{k}\cdot\vec{r}}\tag{3.5}$$

where the coefficients $a_{\vec{k}}$ must be chosen so that $\vec{\nabla}_{\vec{k}} \Psi_{\vec{K}}(\vec{R}, \vec{r}) = i\vec{k} \Psi_{\vec{K}}(\vec{R}, \vec{r})$. (So far all we have done is notational, in order to make what follows plausible.) If we now substitute the wavefunction of Eq. (3.5) into the Schrödinger equation, with the energy defined in Eq. (3.4), we get

$$\left[-\frac{\hbar^2}{m} \left(\vec{\nabla}_{\vec{r}}^2 + \frac{1}{4} \vec{\nabla}_{\vec{R}}^2 \right) + \mathcal{H}_1 \right] \Psi_{\vec{K}}(\vec{R}, \vec{r}) = E \Psi_{\vec{K}}(\vec{R}, \vec{r})\tag{3.6}$$

If we take the dot product of Eq. (3.6) with $\langle e^{-i(\vec{k}\cdot\vec{r} + \vec{K}\cdot\vec{R})} |$ and perform the integrations over \vec{R} and \vec{r} , we get for the kinetic energy term

$$\langle e^{-i(\vec{k}\cdot\vec{r} + \vec{K}\cdot\vec{R})} | -\frac{\hbar^2}{m} (\vec{\nabla}_{\vec{r}}^2 + \frac{1}{4} \vec{\nabla}_{\vec{R}}^2) | \Psi_{\vec{K}'}(\vec{R}, \vec{r}) \rangle = (\epsilon_{K'} + \epsilon_{k'}) \frac{a_{\vec{k}'}}{V}\tag{3.7}$$

and the perturbation term becomes

$$\langle e^{-i(\vec{k}\cdot\vec{r} + \vec{K}\cdot\vec{R})} | \mathcal{H}_1 | \Psi_{\vec{K}'}(\vec{R}, \vec{r}) \rangle = \frac{\delta(\vec{K}' - \vec{K})}{V} \sum_{\vec{k}'} a_{\vec{k}'} \left[\int_{-\infty}^{\infty} d^3r e^{-i\vec{k}\cdot\vec{r}} \mathcal{H}_1 e^{i\vec{k}'\cdot\vec{r}} \right]\tag{3.8}$$

Therefore, if we use the notation $| \vec{k} \rangle$ for a plane wave, the Schrödinger equation may be written as

$$(E - \epsilon_K - \epsilon_k) a_{\vec{k}} = \delta(\vec{K} - \vec{K}') \sum_{\substack{k' \geq q_{\min} \\ k' \leq q_{\max}}} a_{\vec{k}'} \langle \vec{k} | \mathcal{H}_1 | \vec{k}' \rangle\tag{3.9}$$

Since the perturbation \mathcal{H}_1 couples only electrons with k and k' in a small shell around the Fermi surface, Cooper made the approximation that

$$\langle \vec{k}' | \mathcal{H}_1 | \vec{k} \rangle \approx \begin{cases} -|V|, & q_{\min} \leq k, k' \leq q_{\max} \\ 0, & \text{otherwise} \end{cases} \quad (3.10)$$

With this approximation, the Schrödinger equation reduces to

$$a_{\vec{k}} = \frac{-|V|}{(E - \epsilon_K - \epsilon_k)} \sum_{\vec{k}'} a_{\vec{k}'} \quad (3.11)$$

as long as $\vec{K} = \vec{K}'$. Since from normalization we must have

$$\sum_{\vec{k}} a_{\vec{k}} = C, \quad (3.12)$$

Eq. (3.11) becomes

$$\sum_{\vec{k}} a_{\vec{k}} = C = -|V| \sum_{\vec{k}} \frac{C}{(E - \epsilon_K - \epsilon_k)} = -|V| \frac{2C}{(2\pi)^3} \int_{q_{\min}}^{q_{\max}} \frac{d\vec{k}}{(E - \epsilon_K - \epsilon_k)} \quad (3.13)$$

We can change the variable of integration to energy:

$$-|V| \int_{\epsilon_{\min}}^{\epsilon_{\max}} \frac{d\epsilon_k N(E)}{(E - \epsilon_K - \epsilon_k)} = 1$$

and using the fact that the range of the limits of integration is small, we can take the density of states at the Fermi energy $N(E) \approx N(K, E_F)$.

If we then integrate the above equation, and make use of

$$\int dx/x = \ln x \quad \text{and} \quad (3.14)$$

$$\ln x - \ln y = \ln(x/y)$$

we find

$$\exp\left[\frac{1}{N(K, E_F)|V|}\right] = \frac{E - \epsilon_K - \epsilon_{\max}}{E - \epsilon_K - \epsilon_{\min}}. \quad (3.15)$$

Then, by simplifying Eq. (3.15), we get for the energy of the pair

$$E = \epsilon_K + \epsilon_{\min} - \frac{2\hbar\omega_D}{\exp\left[\frac{1}{N(K, E_F)|V|}\right] - 1} \quad (3.16)$$

There are several interesting points to be made about Eq. (3.16), as Cooper himself pointed out. The first is that the energy of the electron pair is lower than that of the individual electrons, and the energy of the pair is lowest if ϵ_K , the center-of-mass energy, is zero. A zero center of mass energy implies that the electrons have both opposite spin and momenta

(see Fig. 2.2); such a state has henceforth been known as a Cooper pair. The energy of such a pair is lower than that of the individual electrons by an amount Δ defined by

$$\Delta = \frac{2\hbar\omega_D}{\exp\left[\frac{1}{N(E_F)|V|}\right] - 1} \approx 2\hbar\omega_D \exp\left[\frac{-1}{N(E_F)|V|}\right] \quad (3.17)$$

where we have neglected the 1 since in the exponential term the product $N(E_F)V$ is small. If $\Delta \approx 2k_B T_c$, then we recover the famous BCS equation for T_c .

What has been presented above is the substance of Cooper's original paper, from which many of the important ideas, if not the details, of the BCS theory can be extracted. The BCS paper makes many useful predictions, and continues today to be widely read because of its great physical content. However, the theory is of limited utility as far as calculation of the properties of actual materials goes, and has been largely supplanted by modern Green's functions methods for first principles calculations. For understanding of the properties of superconducting systems with complex geometries, like layered materials, the phenomenological Ginzburg–Landau theory of superconductivity (see Chapter 2) has proven to be very useful.

3.1.2 Ground State From Cooper Pairs

The preceding section gave a description of a Cooper pair for two electrons in a Fermi sea. BCS took the essential step in providing a full microscopic description of the superconducting state by constructing a ground state wave function in which all the electrons form bound pairs. The BCS approximation to the electronic ground state wave function can be described as follows: group the N conduction electrons into $N/2$ Cooper pairs described by the wave function $\phi(\vec{r}s, \vec{r}'s')$, where \vec{r} is the electronic position and s is the spin quantum number. Then consider the N -electron wave function as a product of $N/2$ identical Cooper pair wave functions

$$\Psi_N(\vec{r}_1s_1, \dots, \vec{r}_Ns_N) = \phi(\vec{r}_1s_1, \vec{r}_2s_2) \cdots \phi(\vec{r}_{N-1}s_{N-1}, \vec{r}_Ns_N). \quad (3.18)$$

Though this state describes a state in which all electrons are bound, in pairs, into identical two electron states, it lacks the symmetry required by the Pauli principle:

$$\Psi_{\text{BCS}} = \mathcal{A}\Psi_N \quad (3.19)$$

where \mathcal{A} is the antisymmetrization operator.

3.1.3 Hamiltonian for the Superconducting Ground State

In this section and the next we shall introduce the theory of the superconducting ground state, which is a part of the microscopic theory of superconductivity published by Bardeen, Cooper, and Schrieffer in 1957. The method of finding the ground state involves

1. devising a Hamiltonian operator, which we do in this section,
2. using an assumed ground-state wave function to find an expression for the energy, and finally
3. minimizing the energy to find the coefficients in the ground-state wave function.

The latter two parts are done in the following section.

The BCS theory is presented in the formalism of second quantization involving creation and annihilation operators. For a systematic introduction to operator algebra, consult a quantum mechanics text.

The equations are written in terms of the creation and annihilation operators introduced earlier for single electrons and now extended to electron pairs. The creation operator $c_{\vec{k}\uparrow}^*$ places an electron in state \vec{k} with spin up, so that if $c_{\vec{k}\uparrow}^*$ operates on the “vacuum” state, in which all \vec{k} states are empty, it produces a new state with one spin-up electron in state \vec{k} :

$$c_{\vec{k}\uparrow}^*|0\rangle = |1_{\vec{k}\uparrow}\rangle \quad (3.20)$$

Likewise, the annihilation operator $c_{\vec{k}\uparrow}$ causes the elimination of an electron in state \vec{k} with spin \uparrow :

$$c_{\vec{k}\uparrow}|1_{\vec{k}\uparrow}\rangle = |0\rangle. \quad (3.21)$$

These operators are used to formulate the Hamiltonian. It is only necessary to consider the differences from the normal ground state, which are referred to as *reduced* energies.

Each electron-phonon-electron interaction of the type shown in Fig. 2.2 and discussed in §3.1.1 contributes to the potential energy of the superconducting state relative to the ground state. As in the Cooper model, we restrict consideration to paired states $\vec{k}\uparrow$, $-\vec{k}\downarrow$. The pair transition can be represented by the product of creation and annihilation operators,

$$c_{\vec{k}+\vec{q}\uparrow}^* c_{-\vec{k}-\vec{q}\downarrow}^* c_{-\vec{k}\downarrow} c_{\vec{k}\uparrow} \quad (3.22)$$

If this operator operates on the ground state, it first removes the electrons from \vec{k} and $-\vec{k}$ states and then places them in $\vec{k}+\vec{q}$ and $-\vec{k}-\vec{q}$ with their spin unaffected. Taking the sum of all such scattering events, one obtains the potential energy relative to the normal state, which we call the reduced potential energy:

$$V_{red} = \sum_{\vec{k}, \vec{q}} V_{\vec{k}\vec{k}'} c_{\vec{k}+\vec{q}\uparrow}^* c_{-\vec{k}-\vec{q}\downarrow}^* c_{-\vec{k}\downarrow} c_{\vec{k}\uparrow} \quad (3.23)$$

where $\vec{k}' = \vec{k} + \vec{q}$. It can be shown that this gives a lowering of the energy for the superconducting state and this lowering of the energy becomes more pronounced as the number of scattering events increases, thus adding justification for using \vec{k} , $-\vec{k}$ pairs.

Since the BCS theory involves only pairs of a certain kind (i.e., $\vec{k}\uparrow$ and $-\vec{k}\downarrow$), single-electron operators are replaced by pair operators

$$b_{\vec{k}}^* = c_{\vec{k}\uparrow}^* c_{-\vec{k}\downarrow}^* \quad (3.24)$$

and

$$b_{\vec{k}} = c_{-\vec{k}\downarrow} c_{\vec{k}\uparrow} \quad (3.25)$$

Since these pairs consist of a spin \uparrow and a spin \downarrow electron, it might be expected that the pairs would behave like bosons. However, this is not strictly the case because the Pauli principle applies: no $\vec{k}\uparrow$, $-\vec{k}\downarrow$ state may be occupied by more than one pair at a time. It does turn out that the pair behavior is close enough to that of a boson so that boson electrodynamics gives a very good representation of the actual behavior of superconductors.

Using Eqs. 3.24 and 3.25, the reduced potential energy in Eq. 3.23 may be rewritten as

$$V_{red} = \sum_{\vec{k}\vec{k}'} V_{\vec{k}\vec{k}'} b_{\vec{k}'}^* b_{\vec{k}} \quad (3.26)$$

The kinetic energy can be written as the sum of the pair energies in each of the occupied pair states. The corresponding Hamiltonian thus must contain the number operator $\hat{n}_{\vec{k}}$ which has the property

$$\hat{n}_{\vec{k}} |n_{\vec{k}}\rangle = n |n_{\vec{k}}\rangle \quad (3.27)$$

which states that the eigenstate of $\hat{n}_{\vec{k}}$ is the state having the wave number \vec{k} and occupancy n , and the eigenvalue of $\hat{n}_{\vec{k}}$ is the occupancy. The number operator in the case of pairs is $b_{\vec{k}}^* b_{\vec{k}}$. Then the pair kinetic energy relative to the Fermi energy is

$$\mathcal{H}_{KE} = 2 \sum_{\vec{k}} \epsilon_{\vec{k}} b_{\vec{k}}^* b_{\vec{k}} \quad (3.28)$$

where $\epsilon_{\vec{k}} = (\hbar^2 k^2 / 2m) - E_F$ is a single particle energy representing the kinetic energy of a Bloch state measured relative to the Fermi level. To express the energy in reduced form (i.e., the kinetic energy relative to the normal ground state), we subtract

$$2 \sum_{k < k_F} \epsilon_{\vec{k}} \quad (3.29)$$

from the kinetic energy given by Eq. 3.28 and the factor of 2 arises because $\epsilon_{\vec{k}}$ denotes the single particle energy for each of the electrons in the pair. This can be done by using the pair commutation relations:

$$[b_{\vec{k}}, b_{\vec{k}'}^*] = [1 - \hat{n}_{\vec{k}\uparrow} - \hat{n}_{-\vec{k}\downarrow}] \delta_{\vec{k}\vec{k}'} \quad (3.30)$$

and the anti-commutator

$$\{b_{\vec{k}}, b_{\vec{k}'}\} = 2b_{\vec{k}} b_{\vec{k}'} (1 - \delta_{\vec{k}\vec{k}'}) \quad (3.31)$$

where the square bracket denotes the commutator $[x, y] = xy - yx$ and the curly bracket denotes the anti-commutator $\{x, y\} = xy + yx$. Performing this operation on Eq. 3.28 and adding to Eq. 3.26, we get the total reduced Hamiltonian:

$$\mathcal{H}_{red} = 2 \sum_{k < k_F} |\epsilon_{\vec{k}}| b_{\vec{k}} b_{\vec{k}}^* + 2 \sum_{k > k_F} \epsilon_{\vec{k}} b_{\vec{k}}^* b_{\vec{k}} + \sum_{\vec{k}'} V_{\vec{k}\vec{k}'} b_{\vec{k}'}^* b_{\vec{k}} \quad (3.32)$$

When operating on the ground state $|0\rangle$ only the operator $b_{\vec{k}}^*$ can yield a non-vanishing result and likewise the operator $b_{\vec{k}}$ is required to operate on an excited state. To explain the factor of 2 in Eqs. 3.28–3.32 another way, these factors of two arise because we count pairs and there are two possible sets of spins for each \vec{k} . The summation considers only the case where we put a spin-up electron in each \vec{k} state and a spin-down electron in the corresponding $-\vec{k}$ state with the factor of 2. Each state for $k < k_F$ contains the full complement of both spin-up electrons and spin-down electrons.

3.1.4 Superconducting Ground State

In this section we use the reduced Hamiltonian Eq. 3.32, to find the distribution of pair occupancy in the superconducting ground state. According to the BCS theory, the ground state should be written as the product of the occupation operators for all pair states.

$$|\Psi\rangle = \prod_{\vec{k}} \left[u_{\vec{k}} + v_{\vec{k}} b_{\vec{k}}^* \right] |0\rangle \quad (3.33)$$

Here $|0\rangle$ is the vacuum state, $v_{\vec{k}}^2$ is the probability of pair occupancy, and $u_{\vec{k}}^2 = 1 - v_{\vec{k}}^2$ is the probability of pair vacancy. The first term in Eq. 3.33 is included since it is needed for normalization of $|\Psi\rangle$. The formation of the BCS ground state of Eq. 3.33 is illustrated in Fig. 3.1 where the successive addition of pairs is schematically shown.

The energy of the superconducting ground state relative to the normal ground state is the expectation value of the reduced Hamiltonian:

$$W = \langle \Psi | \mathcal{H}_{red} | \Psi \rangle \quad (3.34)$$

Substituting Eq. 3.33 and Eq. 3.32 into Eq. 3.34, one obtains

$$W = 2 \sum_{k > k_F} \epsilon_{\vec{k}} v_{\vec{k}}^2 + 2 \sum_{k < k_F} |\epsilon_{\vec{k}}| u_{\vec{k}}^2 + \sum_{\vec{k}\vec{k}'} V_{\vec{k}\vec{k}'} u_{\vec{k}} v_{\vec{k}} u_{\vec{k}'} v_{\vec{k}'} \quad (3.35)$$

To find the equilibrium state we must minimize Eq. 3.35 with respect to $v_{\vec{k}}^2$ by setting $[\partial W / \partial (v_{\vec{k}}^2)] = 0$. The resulting probability of occupancy is found to be

$$v_{\vec{k}}^2 = \frac{1}{2} [1 - \epsilon_{\vec{k}} / (\Delta_{\vec{k}}^2 + \epsilon_{\vec{k}}^2)^{1/2}]. \quad (3.36)$$

The parameter $\Delta_{\vec{k}}$ called the *gap parameter* will be seen in §3.2 to have a special significance and is defined by

$$\Delta_{\vec{k}} = - \sum_{\vec{k}'} V_{\vec{k}\vec{k}'} v_{\vec{k}'} u_{\vec{k}'} \quad (3.37)$$

We can put Eq. 3.36 in a simpler form by defining another energy

$$E_{\vec{k}} = \left(\Delta_{\vec{k}}^2 + \epsilon_{\vec{k}}^2 \right)^{1/2}. \quad (3.38)$$

Using Eq. 3.38 the probability of occupancy (see Eq. 3.36) becomes

$$v_{\vec{k}}^2 = \frac{1}{2} [1 - \epsilon_{\vec{k}} / E_{\vec{k}}] \quad (3.39)$$

which is plotted in Fig. 3.2. This figure shows that the probability of pair occupancy does not vanish above E_F . Pairs move to \vec{k} states of higher kinetic energy [first term in Eq. 3.35] in order to maximize scattering possibilities since that reduces the potential energy [third term in Eq. 3.35] by more than the increase of kinetic energy. The equilibrium distribution is reached when a further increase of kinetic energy is not offset by a decrease of potential energy. The distribution is reminiscent of the normal state with $T \neq 0$; but for the superconducting state, this distribution occurs at $T = 0$. The region of $\epsilon_{\vec{k}}$ over which $v_{\vec{k}}^2$ is significantly different from both unity and zero is of the order of a few $\Delta_{\vec{k}_F}$ (typically, a few milli-electron voly).

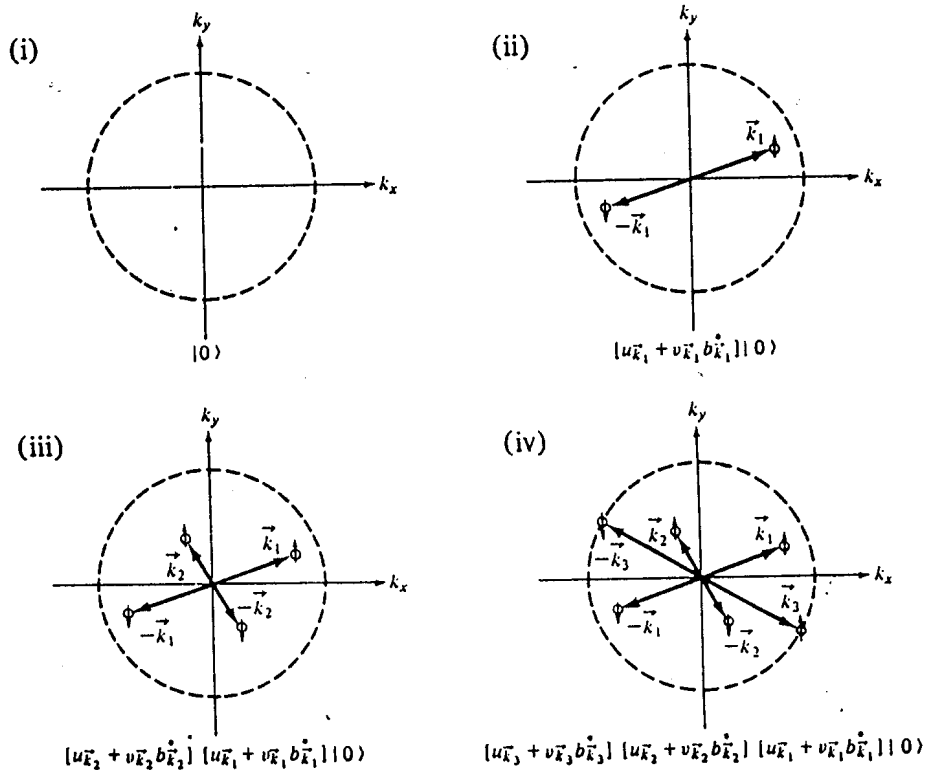


Figure 3.1: Formation of the BCS ground state by successive addition of pairs. Not illustrated are the weighing $v_{\vec{k}}$ of the pairs. The oppositely directed spins are shown. (i) shows the vacuum state and (ii)-(iv) show successive additions of pairs.

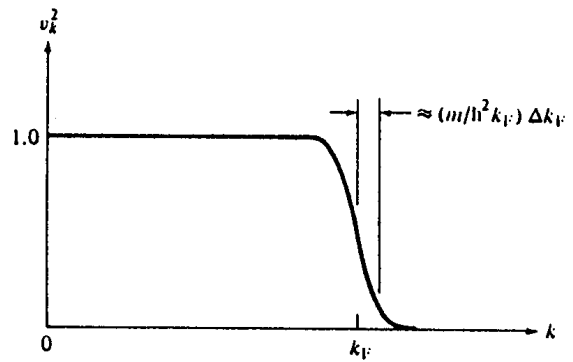


Figure 3.2: Probability of pair occupancy in the superconducting ground state.

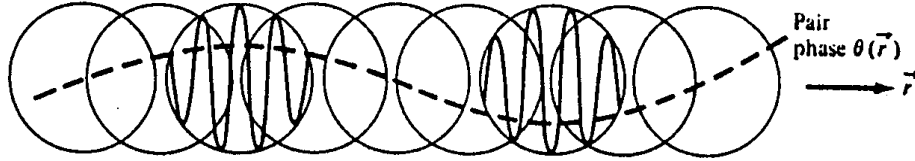


Figure 3.3: The superconducting ground state is composed of a very large number of overlapping Cooper pairs. The phases are locked together to minimize the energy. If there is net momentum, there is a gradient of phase, as illustrated by the dashed line.

3.1.5 Long-range Coherence

The electron occupation of the paired \vec{k} states can be considered to be that of the Cooper pair. Within a spatial region having a diameter on the order of $1 \mu m$, there is a phase coherence much like that in a de Broglie wave packet for a single electron. This distance is called the *coherence length* and is denoted by the symbol ξ . The center-of-mass coordinates of about a million interacting pairs lie within a sphere of diameter ξ . It is energetically favorable for overlapping pairs to lock phases. The whole superconducting fluid can be viewed as consisting of a large number of overlapping pairs. The individual pairs are comprised of a large number of \vec{k} states centered in magnitude about k_F . The resulting wave packet has a wavelength of about one-thousandth of the pair diameter. The waves oscillate at a frequency $\omega = 2E_F/\hbar$. In the absence of a net pair momentum, the phases of all pairs are locked together and they oscillate in unison.

If the pairs of \vec{k} states have a nonzero net wave vector \vec{K} , the wave function representing the superconducting fluid is multiplied by $\exp(i\vec{K} \cdot \vec{r})$. We can represent the fluid by an ensemble-average function $\Psi = |\Psi(\vec{r})|$ when $K = 0$ and by

$$\Psi = |\Psi(\vec{r})| e^{i\vec{K} \cdot \vec{r}} \quad (3.40)$$

when $K \neq 0$. This is usually written in the more general form

$$\Psi = |\Psi(\vec{r})| e^{i\theta(\vec{r})} \quad (3.41)$$

where θ is the phase of the electron pairs, thereby giving a mathematical basis for the ansatz used in Eq. 2.16. Figure 3.3 shows the situation where there is a phase variation, as in Eq. 3.41. In Fig. 3.3 the phases of just two pairs are shown to avoid confusion; the phases of these pairs are seen to differ from one another by 180° . The phases of all the pairs evolve at the angular frequency $2E_F/\hbar$ while maintaining the $\theta(\vec{r})$ relative phase differences.

3.2 Gap Parameter and Condensation Energy at $T = 0$

Let us examine further the gap parameter $\Delta_{\vec{k}}$. Substitution of Eq. 3.39 into Eq. 3.37 gives

$$\Delta_{\vec{k}} = - \sum_{\vec{k}'} V'_{\vec{k}\vec{k}'} \frac{\Delta_{\vec{k}'}}{2E_{\vec{k}'}} \quad (3.42)$$

At this point some simplifying assumptions are made to solve Eq. 3.42. First, we assume that $V_{\vec{k}\vec{k}'} = -V$ if both $|\epsilon_{\vec{k}}|$ and $|\epsilon_{\vec{k}'}|$ are less than $\hbar\omega_D$ and is zero otherwise following Eq. 3.8. It is further assumed that $\Delta_{\vec{k}} = \Delta$, a constant, for $|\epsilon_{\vec{k}}| < \hbar\omega_D$ and is zero otherwise. Thus the quantity in Eq. 3.42 becomes

$$E = (\Delta^2 + \epsilon^2)^{1/2} \quad (3.43)$$

in which Δ taken as a constant and ϵ and E understood to be functions of \vec{k} . Next, the summation over \vec{k}' in Eq. 3.42 is replaced by an integral over the corresponding energy range. Further, we make use of the fact that the density of states is nearly constant close to E_F , so $N(\epsilon) \cong N(0)$ over the range $|\epsilon_{\vec{k}}| < \hbar\omega_D$. With these simplifications, Eq. 3.42 becomes

$$\frac{2}{N(0)V} = \int_{-\hbar\omega_D}^{\hbar\omega_D} \frac{d\epsilon}{[\epsilon^2 + \Delta^2]^{1/2}}. \quad (3.44)$$

Performing the integration in Eq. 3.44 and rearranging terms, we obtain

$$\Delta = \frac{\hbar\omega_D}{\sinh\left[\frac{1}{N(0)V}\right]} \quad (3.45)$$

If $N(0)V \ll 1$, the superconductor has *weak coupling* between electrons and phonons, as is the case in most of the elemental superconducting materials, and in this limit Eq. 3.45 reduces to

$$\Delta = 2\hbar\omega_D \exp\left[\frac{-1}{N(0)V}\right] \quad (3.46)$$

A typical value of Δ for conventional superconductors is about 1 meV.

3.2.1 Condensation Energy

We now calculate the difference in energy between the superconducting and normal states; this is called the energy of condensation into the superconducting state. The difference of kinetic energies is

$$(KE)_s - (KE)_n = 2 \sum_{\vec{k} < \vec{k}_F} |\epsilon_{\vec{k}}| (v_k^2 - 1) + 2 \sum_{\vec{k} > \vec{k}_F} \epsilon_{\vec{k}} v_k^2 \quad (3.47)$$

Using Eqs. 3.38, 3.39 and 3.46 we can rewrite Eq. 3.47 as

$$(KE)_s - (KE)_n = N(0)\Delta^2 \left[\frac{1}{N(0)V} - \frac{(1 - e^{-2/N(0)V})}{2} \right] \quad (3.48)$$

Similarly, the difference of potential energies from Eq. 3.35 is

$$V_s - V_n = -\frac{\Delta^2}{V} \quad (3.49)$$

since $V_n = 0$. The total difference of energies is the sum of Eqs. 3.48 and 3.49. Noting that the change of potential energy is just canceled by the first term of Eq. 3.48 We have the following for the condensation energy:

$$W_s - W_n = -\frac{1}{2}N(0)\Delta^2 \left[1 - e^{-2/N(0)V} \right] \simeq -\frac{1}{2}N(0)\Delta^2 \quad (3.50)$$

A useful physical understanding of Eq. 3.50 can be derived by taking the energy range of pairing interactions to be Δ and noting that the number of pairs in this energy range is about $N(0)\Delta$. If 2Δ to be the binding energy of each electron pair, then the product of the number of pairs and the binding energy is approximately the condensation energy. Thus it is clear that although the BCS theory of the ground state has all electrons paired, only those in a narrow energy range of order Δ participate in the condensation. Those farther below the Fermi level are also described mathematically as pairs but they are too far from the Fermi surface to be scattered by the electron–phonon interaction, and hence do not participate in the reduction of the energy of the system.

3.3 Some Quantitative Predictions of BCS

The BCS theory makes a number of quantitative predictions about observables. We summarize results for the critical temperature, energy gap, critical field and specific heat. At present, many of these observables are being measured for the high T_c materials in an attempt to look for deviations from the BCS theoretical predictions. Agreement with the BCS theory may be explained by the existence of pairs, and for this reason may not provide direct information on whether the pairing mechanism is the electron–phonon interaction or is some other attractive pairing mechanism.

3.3.1 Critical Temperature

In zero field, ordering sets in at a critical temperature T_c given by

$$k_B T_c = 1.13 \hbar \omega_D e^{-1/N_0 V_0} \quad (3.51)$$

No matter how weak the electron-phonon coupling, BCS predicts a transition to a superconducting state for an attractive interaction described by the attractive potential V_0 where N_0 is the density of states at the Fermi level and ω_D is the Debye frequency.

3.3.2 Energy Gap

The zero-temperature energy gap is given by

$$\Delta(0) = 2 \hbar \omega_D e^{-1/N_0 V_0} \quad (3.52)$$

The ratio of Eq. 3.52 to Eq. 3.51 gives a fundamental formula independent of the phenomenological parameters

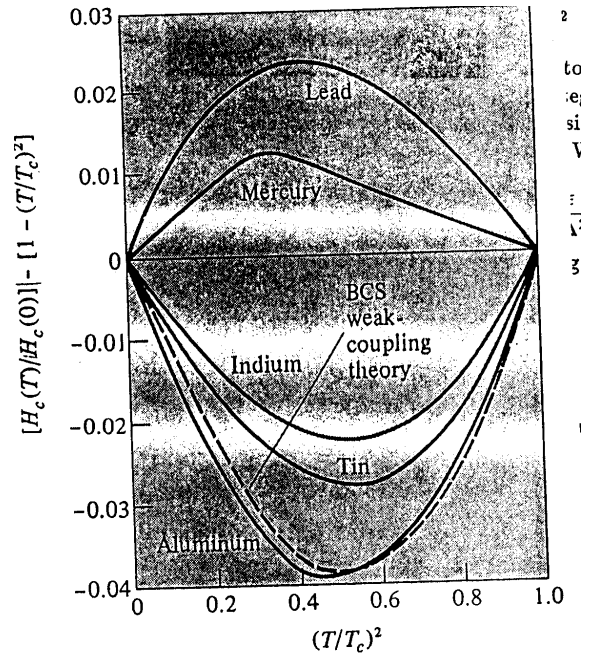
$$\Delta(0) = 1.76 k_B T_c. \quad (3.53)$$

This result seems to hold to within 10% for a large number of superconductors including some of the new high T_c materials, though the results for the high T_c materials must be considered to be preliminary.

The BCS theory also predicts the temperature dependence of the energy gap for T near to T_c as

$$\frac{\Delta(T)}{\Delta(0)} \approx 1.74 \left(1 - \frac{T}{T_c}\right)^{1/2} \quad (3.54)$$

Figure 3.4: The critical field plotted as a deviation from the empirical relation (Eq. 3.55). Measurements are for several metals. The weak-coupling theory of Swihart is shown.



3.3.3 Critical Field

The BCS prediction for $H_c(T)$ is usually expressed in terms of deviations from the empirical law:

$$\frac{H_c(T)}{H_c(0)} \approx 1 - \left(\frac{T}{T_c}\right)^2 \quad (3.55)$$

The BCS prediction is that near T_c the relation is linear

$$\frac{H_c(T)}{H_c(0)} \sim 1.74 \left[1 - \left(\frac{T}{T_c}\right)\right] \quad (3.56)$$

whereas at very low temperatures the prediction is

$$\frac{H_c(T)}{H_c(0)} \sim 1 - 1.06 \left(\frac{T}{T_c}\right)^2. \quad (3.57)$$

Figure 3.4 shows the deviation from Eq. 3.55 for typical type I superconductors where Al is a weak coupling superconductor while Hg and Pb are strong coupling type I superconductors.

The Werthamer–Helfand–Hohenberg (WHH) equation which is also based on the BCS theory

$$H_{c2}(0) = 0.7 \left(\frac{\partial H_{c2}}{\partial T}\right)\Big|_{T_c} T_c \quad (3.58)$$

relates the value of the upper critical field of a typical type II superconductor $H_{c2}(0)$ to the slope at T_c with no adjustable parameters. The WHH formula (Eq. 3.58) works well for isotropic type II superconductors. The application of WHH theory to anisotropic type II high T_c superconductors is currently under investigation.

3.3.4 Specific Heat

BCS predicts a discontinuity at T_c of magnitude

$$\left. \frac{C_s - C_n}{C_n} \right|_{T_c} = 1.43 \quad (3.59)$$

In zero magnetic field. The BCS theory also predicts the low temperature heat capacity which can be written as

$$\frac{C_s}{\gamma T_c} = 1.34 \left(\frac{\Delta(0)}{k_B T} \right)^{3/2} e^{-\Delta(0)/k_B T} \quad (3.60)$$

where γ is the coefficient of the linear specific heat. Equation 3.60 shows that the exponential dependence of the specific heat at low temperature gives a direct measure of the superconducting band gap Δ .

Chapter 4

Superconductivity in High Transition Temperature Cuprate Materials

4.1 Introduction to High T_c Materials

References:

- Tinkham and Lobb, *Solid State Physics*, edited by Ehrenreich and Turnbull, Academic Press, vol **42**, p. 91 (see also other articles in the same volume).
- Poole, Datta and Farach, *Copper Oxide Superconductors*, Wiley–Interscience (1988).
- Phillips, *Physics of High T_c Superconductors*, Academic Press (1989).
- Kamimura and Oshiyama, *Mechanisms of High Temperature Superconductivity*, Springer Series in Materials Science, **11**.
- D.M. Ginsberg, *Physical Properties of High Temperature Superconductors I*, World Scientific (1989).

Using arguments based on the magnitude of the electron–phonon interaction, it was argued that the maximum expected T_c would not exceed $\sim 30\text{K}$. Therefore, the discovery of superconductivity in the lanthanum cuprates ($\text{La}_{2-x}\text{Sr}_x\text{CuO}_4$) in 1986 with T_c values of $\sim 40\text{K}$ and soon thereafter in the $\text{YBa}_2\text{Cu}_3\text{O}_7$ compounds with $T_c \sim 90\text{K}$ was so very surprising. Equally surprising was the discovery of such high T_c 's in materials with magnetic properties and exhibiting insulating phases.

A number of researchers have drawn attention to the fact that almost all high T_c superconductors are layered compounds. The layering introduces anisotropy into the problem which must be considered both in the normal state and in the superconducting state properties. Whereas many of the conventional superconductors are familiar materials that have been studied in depth, the cuprate superconductors relate to much less familiar materials, which are difficult to prepare in stoichiometric, single phase form, and cannot be described theoretically by simple one–electron band theory. We are now at an early stage in our

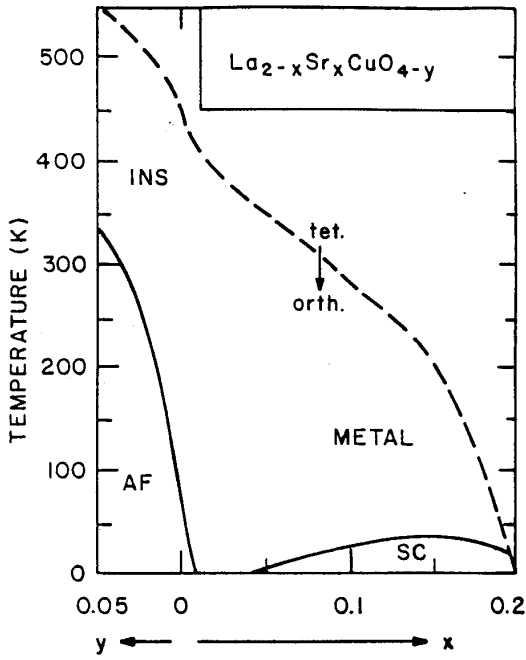


Figure 4.1: A schematic phase diagram for $\text{La}_{2-x}\text{Sr}_x\text{CuO}_{4-y}$. The horizontal axis assumes $y = 0$ when $x \neq 0$ and $x = 0$ when $y \neq 0$. The dashed curve separates tetragonal and orthorhombic structures. The insulator (INS)–metal boundary is not shown because of experimental uncertainties. The diagram shows antiferromagnetic (AF) and superconducting (SC) phases which are common to the various high T_c families: $\text{La}_{2-x}\text{Sr}_x\text{CuO}_{4-y}$, $\text{YBa}_2\text{CuO}_{7-\delta}$, and $\text{Bi}_2\text{Sr}_2\text{Ca}_{1-x}\text{Y}_x\text{Cu}_2\text{O}_{8+y}$.

understanding of the high T_c superconducting materials. The problems are challenging and more difficult than initially envisaged.

It has been suggested that the construction of high T_c superconductors can be engineered from basic building block units, consisting of electrically active slabs between which are sandwiched layers which transfer charge to the electrically active slab. Though we focus here on layered superconductors, it is not clear that all high T_c superconductors are necessarily layered, insofar as the $T_c = 30$ K superconductor BiKBaO is a cubic material which also has no copper ions and thus no magnetism.

All the currently studied high T_c superconductor families seem to follow the common phase diagram shown in Fig. 4.1. Here we see that below a threshold value for the hole concentration x , there is no superconducting state. According to Fig. 4.1, the stoichiometric compounds are all non-conducting antiferromagnets.

To illustrate the basic building blocks of a typical high T_c superconductor, consider the crystal structure for the layered $\text{YBa}_2\text{Cu}_3\text{O}_7$ compound in Fig. 4.2 where each of the layers is labeled. The structure in Fig. 4.2 can be considered in terms of two constituents: the electrically active slab (see Fig. 4.3) which has a chemical formula $\text{YBa}_2\text{Cu}_2\text{O}_6$ and the intercalate layer CuO , where the Cu and O form chains. This intercalate layer allows entry and departure of oxygen, thereby providing a mechanism for creating a hole concentration necessary for observation of the superconducting phase. In Fig. 4.3 we see the basic building blocks and various guest layers that can be introduced between the electrically active $\text{YBa}_2\text{Cu}_2\text{O}_6$ slabs. If a single intercalate layer is introduced, the result is a 90 K T_c material, such as $\text{YBa}_2\text{Cu}_3\text{O}_7$. Various substitutions for Y in terms of a rare earth, or the other substitutions indicated in Fig. 4.3, make little difference to T_c . Insertion of two layers (indicated by the two TlO or BiO layers) give rise to a 110 K T_c material and three layers

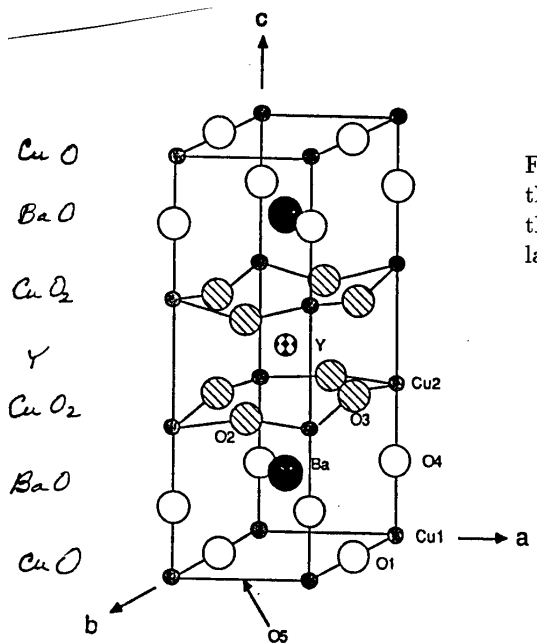


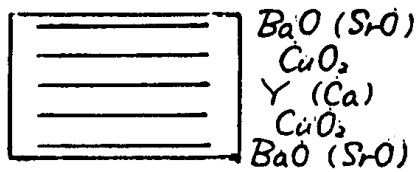
Figure 4.2: The crystal structure of the “123” compound $\text{YBa}_2\text{Cu}_3\text{O}_7$. On the left, the constituents of each of the layers are indicated.

result in a 125 K T_c material (which has been prepared with the Tl compounds). If there is no spacer Y layer between the two CuO_2 layers we have the La_2CuO_4 series which yields a 40 K T_c superconductor. In this case, holes are supplied by the substitution of Sr^{2+} for La^{3+} to yield a family of materials $\text{La}_{2-x}\text{Sr}_x\text{CuO}_4$.

One advantage of viewing the high T_c materials in this way might perhaps be the prediction of new arrangements of the building blocks to achieve higher T_c materials. It is still too soon to be able to judge whether this approach will indeed guide the synthesis of new high T_c materials. It is likely that some new ideas might be needed to produce materials with T_c in the 200 K range.

Most of the high T_c materials are layered compounds with nearly tetragonal crystal structures. In the superconducting phase, they tend to be orthorhombic, but having lattice constants close to those in the corresponding tetragonal phase which is stable at high temperatures. The orthorhombic distortion causes the distance between two oxygens on one diagonal in the CuO_2 planes to be slightly different from the distance between the two oxygens along the other diagonal (see Fig. 4.4).

Because of the basic layering of the crystal structure of the high T_c materials, the critical magnetic fields and the critical currents are also anisotropic in contrast to the simpler superconductors discussed in Chapters 1–3. The transition temperature T_c is a scalar and is unaffected by crystalline anisotropy. It should be emphasized that conventional BCS superconductors can also be anisotropic. On the other hand, since anisotropy is so widespread in the high T_c superconductors, some generalization of the previous discussion of the critical field (see §1.2.1) is necessary. A similar generalization of the critical current concept is also needed.



Electrically active slab

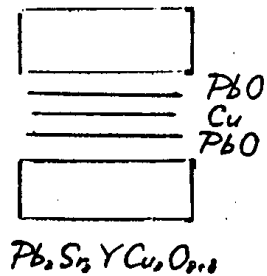
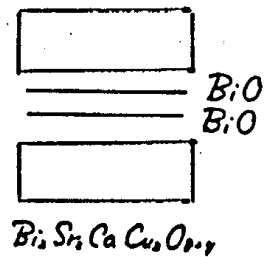
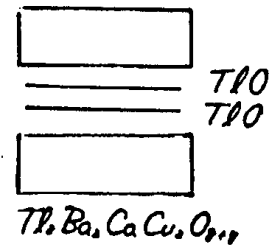
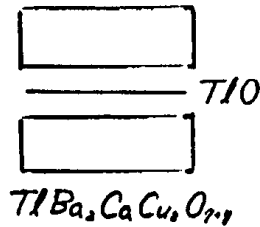
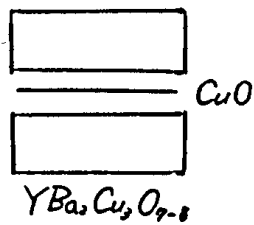


Figure 4.3: Viewing high T_c superconductors in terms of basic building blocks (host material) between which an intercalate layer (or multilayer) is introduced. In general, the larger the number of intercalate layers, the greater the T_c value.

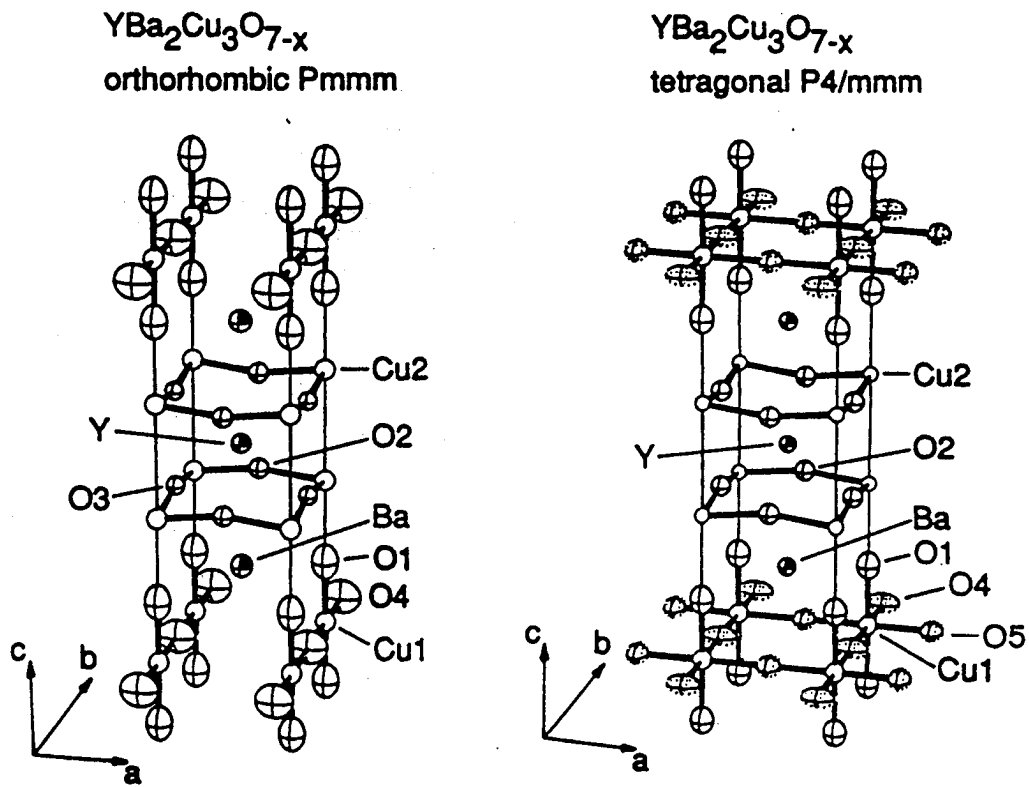


Figure 4.4: Structures of the orthorhombic ($x = 0$) and tetragonal ($x = 0.7$) phases of $\text{YBa}_2\text{Cu}_3\text{O}_{7-x}$.

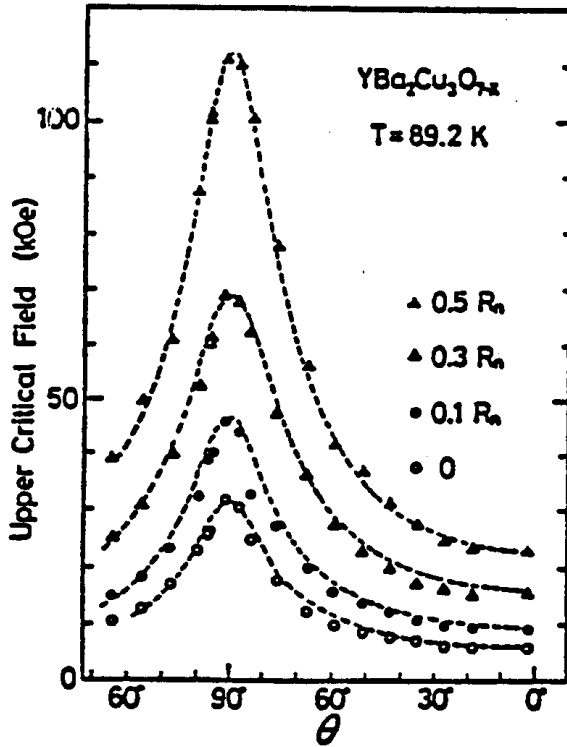


Figure 4.5: Angular dependence of the upper critical fields determined by different criteria, i.e., zero-resistance, 10%, 30% and 50% of the normal resistance. The angle θ denotes the angle of the magnetic field from the c -axis. The dashed curves represent the best fit of Eq. 4.1.

4.2 Anisotropic Superconducting Properties

The superconductivity of single crystal $\text{YBa}_2\text{Cu}_3\text{O}_{7-\delta}$ exhibits a distinct dependence on the magnitude of the magnetic field as well as the field orientation with respect to the crystalline axes. Similar effects are seen in the other families of high T_c superconductors, e.g., $\text{La}_{2-x}\text{Sr}_x\text{CuO}_4$ and $\text{Bi}_2\text{Sr}_2\text{CaCu}_2\text{O}_{8+y}$. This anisotropy of the superconducting properties is seen more clearly in plots of the angular dependence of the upper critical field (see Fig. 4.5). Here, values of the magnetic field at which the resistivity first appears and those at which it reaches 10, 30, 50% are plotted against the angle θ between the magnetic field and the c -axis. Because of the extremely high H_{c2} , especially for $H \perp c$ -axis, data of the sort shown in Fig. 4.5 can be taken for the whole angular range only at temperatures very close to T_c .

The angular dependence of the upper critical field (for all the definitions employed in Fig. 4.5) follows the relation:

$$\left(\frac{H_{c2}(\theta) \cos \theta}{H_{c2}^{\parallel}}\right)^2 + \left(\frac{H_{c2}(\theta) \sin \theta}{H_{c2}^{\perp}}\right)^2 = 1, \quad (4.1)$$

where θ is the angle between the magnetic field and the c -axis direction and H_{c2}^{\parallel} and H_{c2}^{\perp} are the upper critical fields for $H \parallel c$ -axis and that for $H \perp c$ -axis, respectively. The dashed curves in this figure show the good fit of Eq. 4.1 to the experimental points. Although Eq. 4.1 is applicable to many anisotropic conventional (BCS) superconductors, the main difference for the high T_c superconductors as mentioned above is the large magnitude of

H_{c2} , which makes it difficult to carry out the measurements because of the limitations of laboratory fields (~ 30 tesla for dc and ~ 150 tesla for pulsed fields). The critical fields H_{c2}^{\parallel} and H_{c2}^{\perp} of Eq. 4.1 are related (see Eqs. 4.2 and 4.3) to the in-plane and the c -axis coherence lengths, ξ_{ab} and ξ_c by

$$H_{c2}^{\parallel} = \frac{\Phi_0}{2\pi\xi_{ab}^2} \quad (4.2)$$

$$H_{c2}^{\perp} = \frac{\Phi_0}{2\pi\xi_{ab}\xi_c}. \quad (4.3)$$

From these expressions we can expect that as H_{c2} increases to very large values, the coherence lengths become small. Small ξ values ($\xi_c \approx 3\text{\AA}$ and $\xi_{ab} \approx 10\text{\AA}$) and high anisotropy ratios (ξ_{ab}/ξ_c) ~ 5 are characteristic of high T_c materials. The effective mass model (not discussed in these lectures) is applicable to the case where the anisotropy is not too large and the superconductivity can essentially be treated as three-dimensional. The H_{c2} anisotropy is then related to the effective mass anisotropy by

$$\frac{H_{c2}^{\perp}}{H_{c2}^{\parallel}} = \frac{\xi_{ab}}{\xi_c} = \left(\frac{m_c}{m_{ab}}\right)^{1/2} \quad (4.4)$$

where m_{ab} and m_c are the in-plane and c -axis effective masses, respectively. In the simple case where the conductivity anisotropy is also determined by the mass anisotropy, the relation $(H_{c2}^{\perp}/H_{c2}^{\parallel})^2 \sim (\rho_c/\rho_{ab})$ is expected to hold. These relations between the superconducting and normal state parameters seem to hold well for the $\text{YBa}_2\text{Cu}_3\text{O}_{7-\delta}$ family of high T_c superconductors, at least, as reported by some workers.

Another phenomenological model for the angular dependence of $H_{c2}(\theta)$ is the Tinkham model for a thin film superconductor, in which $H_{c2}(\theta)$ is given implicitly by the relation

$$\left(\frac{H_{c2}(\theta)\sin\theta}{H_{c2}^{\perp}}\right)^2 + \left|\frac{H_{c2}(\theta)\cos\theta}{H_{c2}^{\parallel}}\right| = 1. \quad (4.5)$$

Equation 4.5 was introduced to explain the critical anisotropy for thin film superconductors. Equation 4.5 seems to be more appropriate than Eq. 4.1 for the more two-dimensional family of high T_c superconductors $\text{BiSr}_2\text{CaCu}_2\text{O}_{8+x}$ (Bi-1212) which have a larger anisotropy than $\text{YBa}_2\text{Cu}_3\text{O}_{7-\delta}$. A distinct feature of the Tinkham model is that $H_{c2}(\theta)$ shows a cusp at $\theta = \pi/2$ (i.e., for $\vec{H} \perp c$ -axis). In practice, inhomogeneities in the high T_c samples make it difficult to identify such features uniquely.

The temperature dependence of the resistivity for various values of the magnetic field are shown in Fig. 4.6 and permit an evaluation of the temperature dependence of H_{c2}^{\parallel} and H_{c2}^{\perp} . Two sets of H_{c2} data corresponding to different definitions for T_c are shown in Fig. 4.7. The circle points associated with the solid curves in Fig. 4.7 are those defined by the zero-resistance points, and the triangles associated with the dashed curves are those defined by the mid-points of the resistive transition.

Tinkham and coworkers have fit the resistivity vs. temperature curves in Fig. 4.6 to a model based on an activation energy, associated with the energy to unpin a vortex bound to a defect. For practical applications of type II superconductors, strong vortex pinning is necessary. The technology of solving the flux pinning problem in high T_c superconductors is a major challenge with regard to practical utilization of these materials. Likewise, the

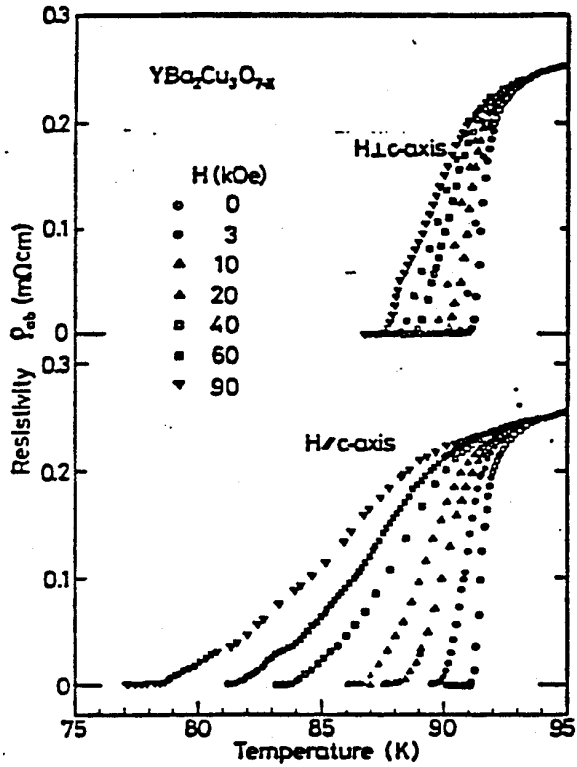


Figure 4.6: Temperature dependence of the ab -plane resistivity at various magnetic field values of a $\text{YBa}_2\text{Cu}_3\text{O}_{7-\delta}$ single crystal in magnetic fields applied parallel and perpendicular to the c -axis (Iye et al., *Physica C* **153–155**, 26 (1988)).

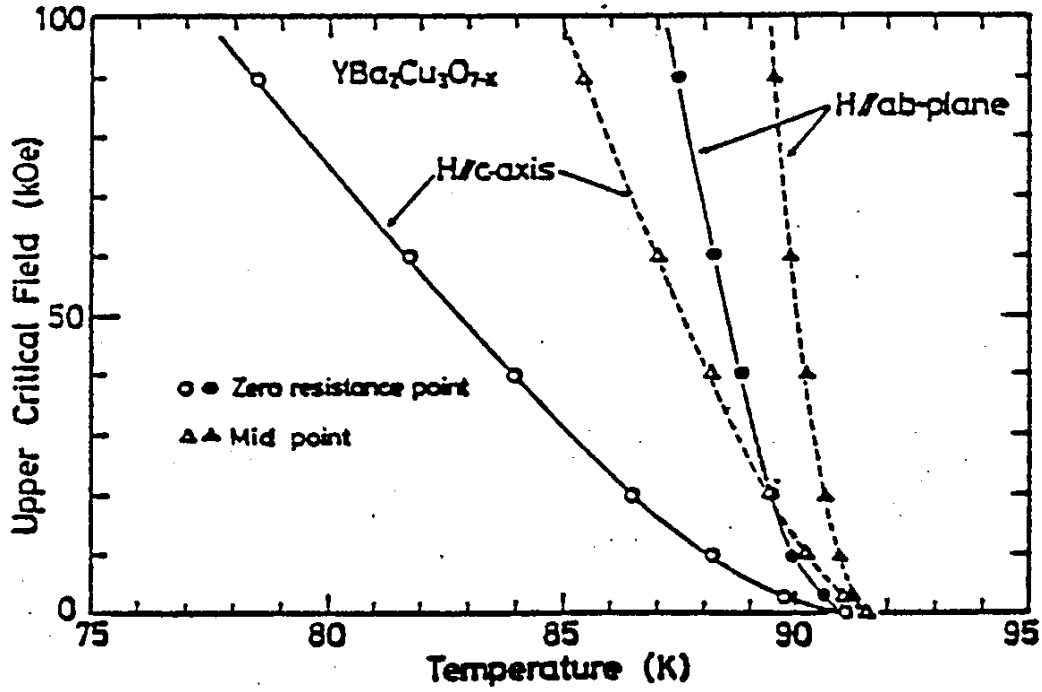


Figure 4.7: Temperature dependence of H_{c2}^{\parallel} and H_{c2}^{\perp} , defined by the zero-resistance points and the mid-points. These $H_{c2}(T)$ data show positive curvature characteristic of many layered superconductors, but otherwise not generally found. The estimated coherence lengths are $\xi_{ab} \sim 25\text{\AA}$ and $\xi_c \sim 6.3\text{\AA}$ from the zero-resistance curves, and $\xi_{ab} \sim 17\text{\AA}$ and $\xi_c \sim 3.9\text{\AA}$ from the mid-point curves (Iye et al., *Physica C*153–155, 26 (1988)).

technology to produce practical high T_c materials with high current carrying capacity (i.e., high j_c) is another major challenge.

In the framework of the Ginzburg-Landau (GL) theory, the temperature dependence of H_{c2} is given by the temperature dependence of the coherence length $\xi(T)$ which has a mean field form

$$\xi(T) \sim (1 - T/T_c)^{-1/2}. \quad (4.6)$$

A Taylor expansion of $H_{c2}(T)$ about T_c yields a linear temperature dependence of H_{c2} near T_c

$$H_{c2}^{\parallel} = |dH_{c2}^{\parallel}/dT|_{T_c} \cdot (T_c - T), \quad (4.7)$$

$$H_{c2}^{\perp} = |dH_{c2}^{\perp}/dT|_{T_c} \cdot (T_c - T), \quad (4.8)$$

where $|dH_{c2}^{\parallel}/dT|_{T_c}$ and $|dH_{c2}^{\perp}/dT|_{T_c}$ are the critical field slopes near T_c . Further assumptions are needed to obtain $H_{c2}(T)$ over a wider temperature range.

A method widely employed in deriving the low temperature coherence lengths is to estimate $H_{c2}^{\parallel}(0)$ and $H_{c2}^{\perp}(0)$ using the Werthamer-Helfand-Hohenberg (BCS) formula for a

type II superconductor

$$H_{c2}(0) = 0.69 \left| \frac{dH_{c2}}{dT} \right|_{T_c} \cdot T_c \quad (4.9)$$

for both H_{c2}^{\parallel} and H_{c2}^{\perp} , where the zero temperature values are deduced from the slope of the critical field curves near T_c . This formula unfortunately does not work well for layered conventional superconductors. But since ordinarily available laboratory magnetic fields are not large enough to probe H_{c2} at low temperatures, Eq. 4.9 is used to obtain rough estimates for H_{c2} near $T = 0$ (recently H_{c2} has been measured directly using megagauss fields available at the University of Tokyo). From Eq. 4.9, the measurements of H_{c2} near T_c can be used to estimate $\xi_{ab}(0)$ and $\xi_c(0)$ using Eqs. 4.2 and 4.3. Experiments in $\text{YBa}_2\text{Cu}_3\text{O}_7$ by Worthington et al. estimated $H_{c2}^{\perp} \sim 64$ tesla and $H_{c2}^{\parallel} \sim 400$ tesla which correspond to $\xi_{ab} \sim 17\text{\AA}$ and $\xi_c \sim 3.5\text{\AA}$.

The experimental determination of $H_{c2}(0)$ and $\xi(0)$ in high T_c superconductors is ambiguous to some degree because of the broadening of the resistive transition in magnetic fields (see Fig. 4.7) and the upward curvature of $H_{c2}(T)$ (i.e., $\partial^2 H_{c2}(T)/\partial T^2 > 0$) near T_c . The values of the coherence length extracted from the H_{c2} measurements appear to lie in the range, $15 < \xi_{ab} < 35$ Å and $2 < \xi_c < 7$ Å, for $\text{YBa}_2\text{Cu}_3\text{O}_{7-\delta}$. For such small values for the c-axis coherence lengths, we see that ξ_c is comparable to or less than the corresponding unit cell distances. $\text{BiSr}_2\text{CaCu}_2\text{O}_{8+x}$ shows a larger H_{c2} anisotropy and a shorter c-axis coherence length compared with $\text{YBa}_2\text{Cu}_3\text{O}_{7-\delta}$ indicating that the former is more two-dimensional, a result consistent with the resistivity anisotropy data.

4.3 Anisotropic Normal State Transport Properties

A great deal of work has been done on all properties of high T_c materials in normal and superconducting state: transport, thermal, optical, lattice, magnetic, elastic, microwave, to mention a few. We briefly discuss transport to give some perspective on the difficulties of these studies.

The anisotropic superconducting properties arise from anisotropic normal state properties. An overall view of the temperature dependence of the normal state resistivities of $(\text{La}_{1-x}\text{Sr}_x)_2\text{CuO}_4$ and $\text{YBa}_2\text{Cu}_3\text{O}_{7-\delta}$ (see Fig. 4.8) show that the ρ values are rather high for metallic systems but $\rho(T)$ still exhibits a remarkably large linear T metallic behavior over a wide temperature range. Figure 4.8 presents a comparison of the temperature dependences of the normal state resistivity of high T_c compounds with those of a weak electron–phonon coupling metal (Cu) and a strong electron–phonon coupling metal (V_3Si) showing saturation in the resistivity $\rho(T)$ at high temperatures. The absence of resistivity saturation in the high T_c superconductors at higher temperatures indicates that the carrier mean free path is longer than the atomic distance throughout the whole temperature range. From this result it is concluded that the electron–phonon coupling in high T_c superconductors is weaker than that in the A15 superconductors which have high T_c values in comparison to most conventional superconductors.

The first measurement of the normal state resistivity anisotropy in $\text{YBa}_2\text{Cu}_3\text{O}_{7-\delta}$ (made with electrical contacts at the four corners of a c -axis containing facet of a single crystal sample) showed a metallic linear T dependence for the ab -plane resistivity, ρ_{ab} , but the c -axis resistivity, ρ_c , showed a semiconductor-like temperature dependence. The anisotropy

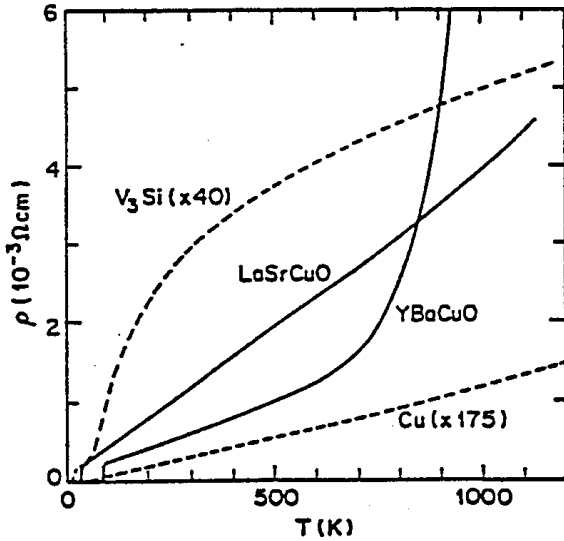


Figure 4.8: Comparison of the temperature dependence of the resistivity of the high T_c superconductors with typical metals. The linear T dependence of the resistivities of $(\text{La}_{1-x}\text{Sr}_x)_2\text{CuO}_4$ and $\text{YBa}_2\text{Cu}_3\text{O}_{7-\delta}$ are in marked contrast with the resistivity saturation in the strong electron-phonon coupling metal V_3Si . Also note the high values of ρ for the high T_c materials in the normal state. The increase in the resistivity of $\text{YBa}_2\text{Cu}_3\text{O}_{7-\delta}$ above ~ 600 K is due to oxygen desorption (M. Gurvitch and A.T. Fiory, *Phys. Rev. Lett.* **59**, 1337 (1987)).

ratio ρ_c/ρ_{ab} was about 30 at room temperature and increased to ~ 80 at T_c . More detailed results (K. Murata, K. Hayashi, Y. Honda, M. Tokumoto, H. Ihara, M. Hirabayashi, N. Terada and Y. Kimura, *Jpn. J. Appl. Phys.* **26**, L1941 (1987)) as shown in Fig 4.9 stimulated a great deal of theoretical interest.

Anderson and Zou (P.W. Anderson and Z. Zou, *Phys. Rev. Lett.* **60**, 132 (1988)) proposed that the ρ_c data shown in Fig. 4.9 could be fitted to a functional form

$$\rho_c(T) = AT + \frac{B}{T}. \quad (4.10)$$

and claimed that the behavior $\rho_{ab} \sim T$ and $\rho_c \sim 1/T$ approximately fits the holon-spinon transport scheme of the “resonating valence bond” (RVB) theory. The scenario for transport in the RVB model is as follows.

The spin degrees of freedom in the two-dimensional CuO_2 network are carried by Fermion excitations called spinons. Chemical doping produces a hole which introduces a spin $1/2$ and a charge $+1$ into the system. These charge and spin degrees of freedom are decoupled in the RVB model to yield a spinon and a positively charged Boson called a holon. Transport current within each CuO_2 plane is carried by holons. The dominant scatterers for a holon are thermally excited spinons. The number of thermally excited spinons is proportional to T , from which the linear T dependence of the in-plane resistivity arises. On the other hand, transport along the c -axis involves interlayer tunneling of electrons. Because a holon is an entity only meaningful within each CuO_2 layer, the interlayer tunneling requires real holes. The tunneling process therefore occurs by

- creation of a real hole by the temporary union of a holon and a spinon
- interlayer tunneling of the real hole
- dissociation of the hole to a holon and a spinon in the new layer.

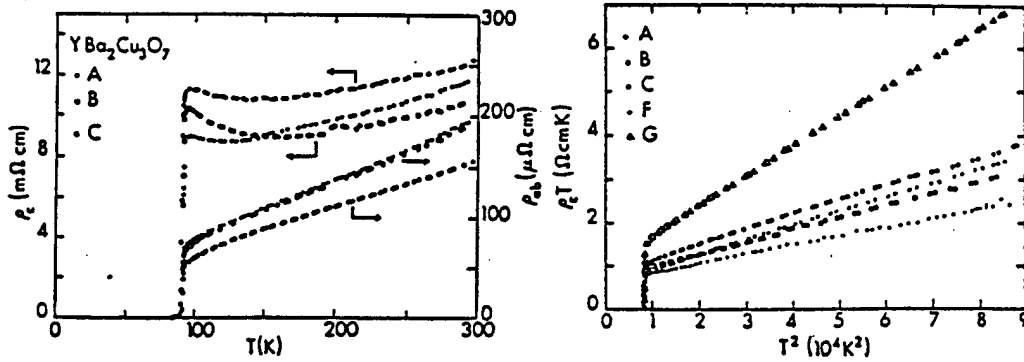


Figure 4.9: Temperature dependence of ρ_{ab} and ρ_c of three single crystals (A, B, C) of $\text{YBa}_2\text{Cu}_3\text{O}_{7-\delta}$. The $\rho_c(T)$ curves show an upturn near T_c . The right hand side of the figure shows the $\rho_c T$ versus T^2 plot which was interpreted to support the validity of Anderson's RVB relation $\rho_c = AT + B/T$ (Hagen et al., *Phys. Rev.* **B37**, 7928 (1988)).

The probability of the interlayer tunneling is determined by the frequency at which a holon encounters a spinon, and therefore is proportional to the number of available spinons. Thus, for the transport along the c -axis, the conductivity rather than the resistivity is proportional to T .

Figure 4.10 shows more recent experimental results by Iye et al. of ρ_{ab} and ρ_c for two different single crystal samples of $\text{YBa}_2\text{Cu}_3\text{O}_{7-\delta}$. These results clarify previous work. Whether the intrinsic $\rho_c(T)$ is metallic or semiconductor-like is extremely important, because the latter result strongly suggests the RVB transport mechanism. The current experimental situation of the anisotropic resistivity of $\text{YBa}_2\text{Cu}_3\text{O}_{7-\delta}$ may be summarized as follows:

- There is general consensus on the following two points:
 1. ρ_{ab} increases linearly with temperature from T_c up to ~ 600 K. The behavior above ~ 600 K is related to oxygen desorption and therefore depends on the ambient oxygen pressure and diffusion kinetics. The linear T dependence extrapolation to $T = 0$ gives a very small intercept for good samples.
 2. ρ_c of an oxygen-deficient sample is semiconductor-like. In the case of a highly oxygen-deficient non-superconducting sample, both ρ_{ab} and ρ_c are of course semiconductor-like.
- The controversial point is whether the $\rho_c(T)$ of an ideally oxygenated sample is metallic or semiconductor-like.
 1. Those who regard the semiconductor-like behavior of ρ_c as intrinsic attribute the metallic behavior observed by others to electrical shorting by ρ_{ab} components due to imperfect crystallinity.
 2. Those who think that the intrinsic ρ_c is metallic, regard the semiconductor-like data as a sign of presence of a microcrack and/or a poorly oxygenated interior

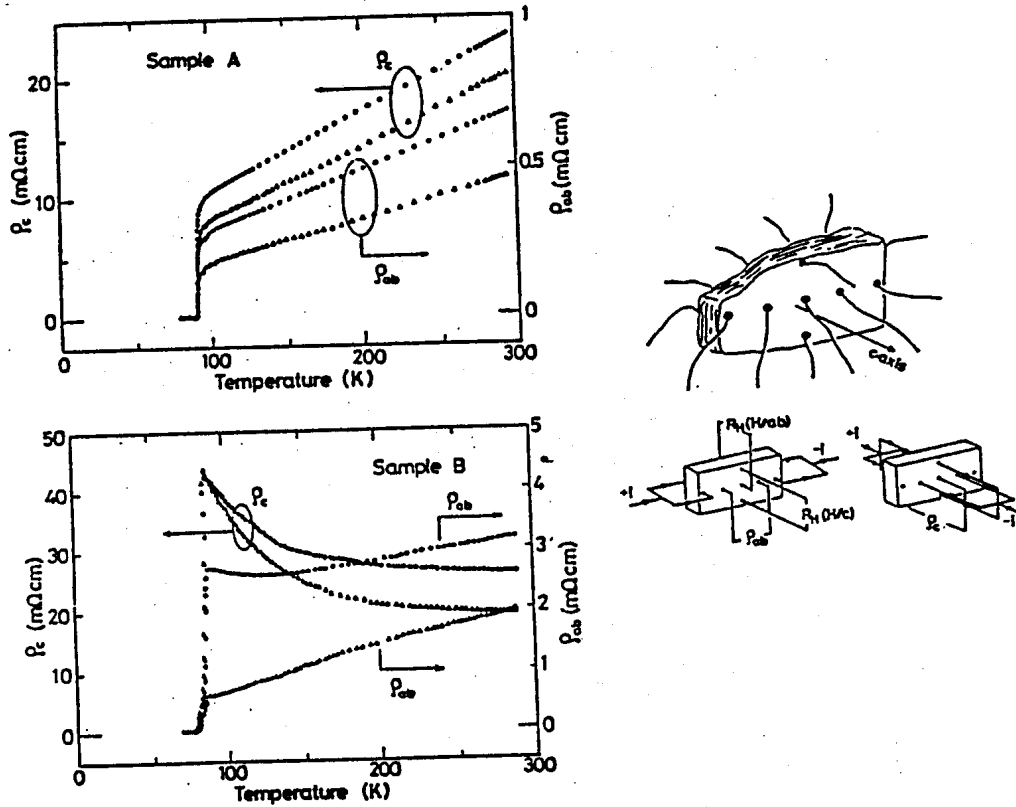


Figure 4.10: Temperature dependence of ρ_{ab} and ρ_c for two single crystal samples of $\text{YBa}_2\text{Cu}_3\text{O}_{7-\delta}$ with different oxygen stoichiometries. Sample A is a fully oxygenated sample, while sample B is a somewhat oxygen-deficient sample. The fully oxygenated sample shows a metallic ρ_{ab} and ρ_c . The right hand side of the figure illustrates the electrode configuration for the measurements of various transport coefficients (Iye et al., *Physica C* **153–155**, 26 (1988)).

region of a single crystal.

The disparity of the experimental data among different groups obviously stems from the strong dependence of electronic properties on the oxygen stoichiometry and from the difficulty of preparing defect-free large single crystals with controlled oxygen stoichiometry. Because the oxygen diffusion kinetics in single crystals is many orders of magnitude slower than in the case of sintered polycrystals, it is necessary to exercise great care when processing a single crystal by oxygen annealing to ensure uniform oxygen concentration. An oxygen concentration gradient from surface to interior of a single crystal can severely distort transport measurements.

An accurate determination of the anisotropy ratio ρ_c/ρ_{ab} is very difficult experimentally. The two-dimensionality of the transport phenomena would seem to require a larger anisotropy than has yet been reported (e.g., $\rho_c/\rho_{ab} > 10^4$ would strongly suggest 2D behavior). The anisotropies reported to date suggest that the high T_c superconductors are all anisotropic 3D materials as far as their normal state properties are concerned.

Let us now briefly review the results on other cuprates. While large single crystals of the undoped material La_2CuO_4 are available, high quality single crystals of the Sr doped materials $\text{La}_{2-x}\text{Sr}_x\text{CuO}_4$ are difficult to grow. The anisotropic resistivity of superconducting single crystals of $\text{La}_{2-x}\text{Sr}_x\text{CuO}_{4-y}$ ($x \sim 0.08$) were measured and the data show an upturn of ρ_c at lower temperatures and the anisotropy of $\rho_c/\rho_{ab} \sim 10$. A few studies on the resistivity anisotropy of $\text{Bi}_2\text{Sr}_2\text{CaCu}_2\text{O}_{8+x}$ single crystals were recently published and were reported to both show metallic behavior with an extremely large anisotropy ratio ($\sim 10^5$). However other experimentalists disagree, so the case of $\text{Bi}_2\text{Sr}_2\text{CaCu}_2\text{O}_{8+x}$ is similar to that of $\text{YBa}_2\text{Cu}_3\text{O}_{7-\delta}$ where significant experimental questions remain to be resolved.

A number of optical experiments have been made on high T_c superconductors. A scaling between T_c and the plasma frequency is shown in Fig. 4.11. These results show a clear correlation between T_c and ω_p^2 , which in turn depends on the hole concentration.

4.4 The Hall Effect in High T_c Materials

Hall effect measurements have been helpful in distinguishing between the carrier density and mobility contributions to the electrical conductivity and in determining the sign of the dominant carrier type. Because of the high anisotropy of the transport properties, single crystal samples are needed to obtain definitive information (see Fig. 4.12).

Early measurements of the Hall constant \mathcal{R}_H with Sr doped $\text{La}_{2-x}\text{Sr}_x\text{CuO}_4$ showed a positive sign of \mathcal{R}_H and the functional dependence $1/\mathcal{R}_H \sim x$ which contradicted the prediction of the band model and suggested that electron correlation is essential in understanding the electronic structure of the present system. Similar conclusions were reached by studies of the variation of the Hall constant with oxygen-deficiency δ in the $\text{YBa}_2\text{Cu}_3\text{O}_{7-\delta}$ system.

The ab -plane Hall coefficient of $\text{YBa}_2\text{Cu}_3\text{O}_{7-\delta}$ has the following features:

1. The sign of the Hall coefficient \mathcal{R}_H is positive, i.e., hole-like.
2. \mathcal{R}_H is very sensitive to the oxygen stoichiometry and increases rapidly with increasing oxygen-deficiency δ .

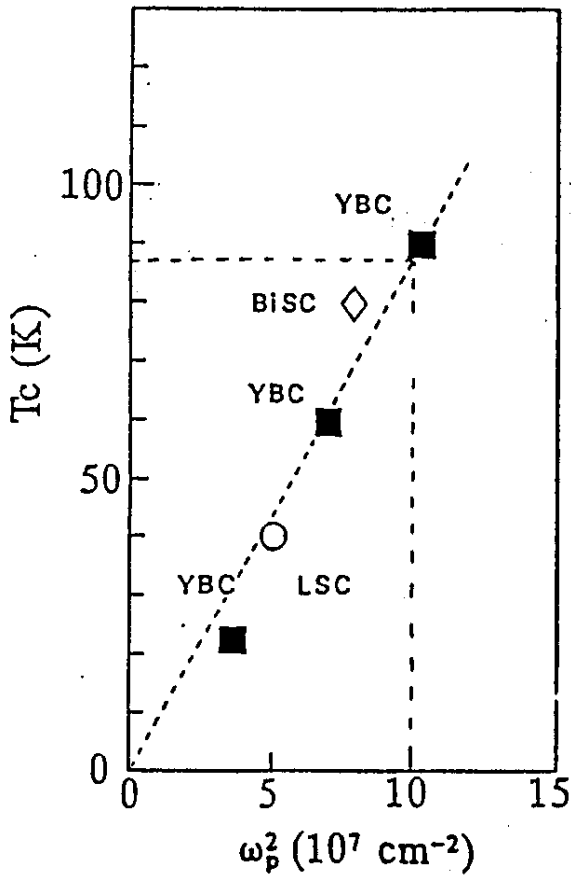


Figure 4.11: The plasmon dependence of T_c . The points labeled BiSC refer to $\text{Bi}_2\text{Sr}_2\text{CaCu}_2\text{O}_{8+x}$, those labeled YBC refer to $\text{YBa}_2\text{Cu}_3\text{O}_{7-\delta}$, while those labeled LSC refer to $\text{La}_{2-x}\text{Sr}_x\text{CuO}_4$.

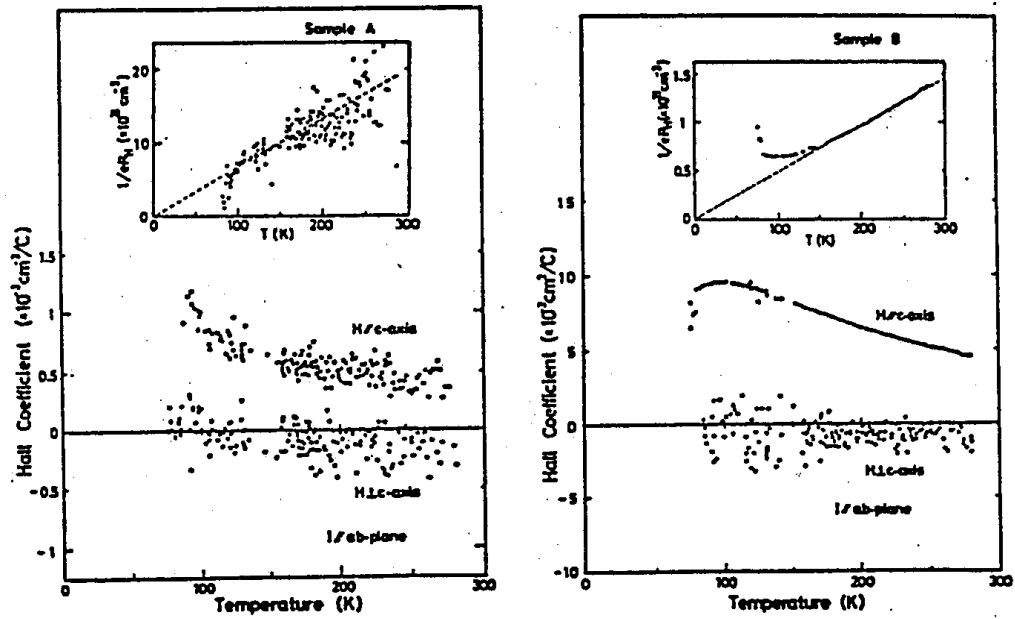


Figure 4.12: Temperature dependence of the anisotropic Hall coefficient \mathcal{R}_H of the same two single crystals of $\text{YBa}_2\text{Cu}_3\text{O}_{7-\delta}$ as in Fig. 4.10. The Hall coefficient for $\vec{H} \parallel ab$ -plane and $\vec{H} \parallel c$ -axis show a striking difference in sign and temperature dependence. The insert shows the characteristic linear T behavior of $1/\mathcal{R}_H$ of $\text{YBa}_2\text{Cu}_3\text{O}_{7-\delta}$ for two crystals with widely different carrier concentrations (Iye et al., *Physica* **C153–155**, 26 (1988)).

3. \mathcal{R}_H exhibits a striking temperature dependence. For well oxygenated samples (90 K superconductors) the temperature dependence is such that the apparent carrier density $1/e\mathcal{R}_H$ varies linearly with T extrapolating to nearly zero at $T = 0$.

The Hall coefficient of polycrystalline samples essentially reflects that of single crystals for the experimental configuration $\vec{j} \parallel ab$ -plane and $\vec{H} \parallel c$ -axis.

The insert figures in Fig. 4.12 demonstrate the linear T dependence of $1/e\mathcal{R}_H$. Normally, \mathcal{R}_H for metals has a linear T dependence. The unusual temperature dependence of Fig. 4.12 is commonly observed in $\text{YBa}_2\text{Cu}_3\text{O}_{7-\delta}$ samples, including samples with very different magnitudes of the Hall constant (due to different oxygen contents). A linear temperature dependence for $1/e\mathcal{R}_H$ would imply a diminishing carrier concentration at low temperatures, a strange occurrence for a metallic system. Moreover, essential constancy of the carrier concentration has been established by the penetration depth measurements by the muon spin rotation technique. Therefore, different interpretations have been proposed for the linear T dependence of $1/e\mathcal{R}_H$.

Using a two-band model, the resistivity and the Hall mobility are expressed in terms of the densities n_e and n_h and mobilities μ_e and μ_h of electrons and holes:

$$\rho = \frac{1}{(n_h|e|\mu_h + n_e|e|\mu_e)} \quad (4.11)$$

$$\mathcal{R}_H = \frac{(n_h\mu_h^2 - n_e\mu_e^2)}{|e|c(n_h\mu_h + n_e\mu_e)^2} \quad (4.12)$$

In this model the temperature dependence of \mathcal{R}_H reflects a temperature dependent compensation between electrons and holes. It is not generally possible to uniquely determine the values of the parameters n_e , n_h , μ_e and μ_h from experimental data of $\mathcal{R}_H(T)$ and $\rho(T)$. It has been recognized that in order to reproduce the $\mathcal{R}_H \sim 1/T$ and $\rho \sim T$ behavior in terms of the two-band model one has to assume a very unusual special relation among the parameters. The lack of a pressure dependence of \mathcal{R}_H poses a further constraint on the simple two-band model. At present, the Hall effect data for $\text{YBa}_2\text{Cu}_3\text{O}_{7-\delta}$ remain to be fully elucidated.

Temperature dependent Hall measurements have also been observed in $\text{La}_{2-x}\text{Sr}_x\text{CuO}_4$ and $\text{Bi}_2\text{Sr}_2\text{CaCu}_2\text{O}_{8+x}$, though the temperature dependence of \mathcal{R}_H is much weaker than for $\text{YBa}_2\text{Cu}_3\text{O}_{7-\delta}$ and what is more important, the unusual behavior of $1/\mathcal{R}_H \sim T$ is not observed. Since the $1/\mathcal{R}_H \sim T$ behavior may be specific to $\text{YBa}_2\text{Cu}_3\text{O}_{7-\delta}$, it is concluded that this effect probably does not have a direct relation to the mechanism of high temperature superconductivity. It may be that the $1/\mathcal{R}_H \sim T$ behavior is common to many high T_c compounds and is a sign of the unconventional normal state from which high temperature superconductivity emerges. Whether this unusual T dependence of the Hall constant can be explained within the framework of relatively conventional models or requires an exotic conduction mechanism (e.g., RVB) remains to be clarified.

Our current knowledge of the anisotropy of the Hall effect in $\text{YBa}_2\text{Cu}_3\text{O}_{7-\delta}$ may be summarized as follows:

1. The Hall effect for $\vec{H} \parallel c$ -axis is positive and $1/e\mathcal{R}_H$ varies linearly with temperature.
2. \mathcal{R}_H for $\vec{H} \parallel ab$ -plane is much smaller than that for $\vec{H} \parallel c$ -axis, which is the reason why the Hall data on ceramic samples essentially reflect the latter.

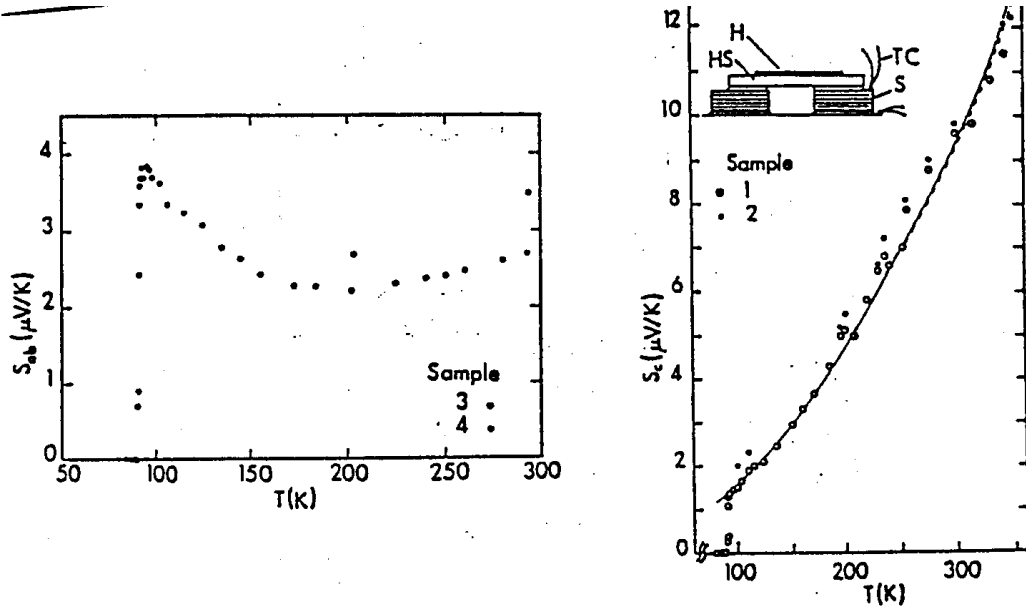


Figure 4.13: Temperature dependence of the anisotropic thermoelectric power of single crystal samples of $\text{YBa}_2\text{Cu}_3\text{O}_{7-\delta}$. Note the qualitative difference in the temperature dependence for the two directions of heat flow.

3. \mathcal{R}_H for $\vec{H} \parallel ab$ -plane is negative and seems to have a temperature dependence quite different from that for $\vec{H} \parallel c$ -axis.

Such a complicated dependence of the Hall effect on the magnetic field orientation implies a complicated Fermi surface topology, or may provide evidence for an exotic transport mechanism along with the unusual temperature dependence.

The anisotropy of the thermoelectric power of $\text{YBa}_2\text{Cu}_3\text{O}_{7-\delta}$ has been measured by a few groups (Ong et al., *Physica* **C153–155**, 1072 (1988)), but the results are not in good agreement from one group to another. Some authors show a positive thermopower for both S_{ab} and S_c (see Fig. 4.13) while other authors show $S_{ab} < 0$ and $S_c > 0$. There is however agreement that the functional form of the temperature dependence $S_{ab}(T)$ is very different from $S_c(T)$.

Thermal conductivity experiments have also been carried out on both single crystal and polycrystalline of oxygen-deficient $\text{La}_2\text{CuO}_{4-y}$ samples (see Fig. 4.14), showing interesting magnon contributions to the thermal conductivity and a high degree of anisotropy.

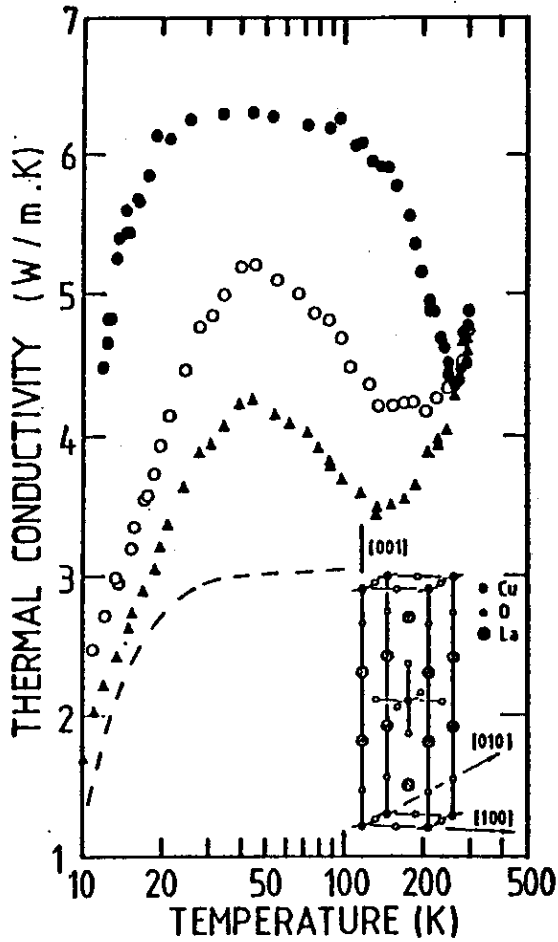


Figure 4.14: Thermal conductivity of single crystal $\text{La}_2\text{CuO}_{4-y}$ for the heat flow $Q \parallel [001]$ (top, closed circles), $Q \parallel [221]$ (middle, open circles) and $Q \parallel [110]$ (bottom, triangles). The dashed line represents results on a polycrystalline sintered sample. The inset shows a schematic diagram of $\text{La}_2\text{CuO}_{4-y}$ in terms of the tetragonal coordinate system used (D.T. Morelli, J. Heremans, G.L. Doll, P.J. Picone, H.P. Jenssen and M.S. Dresselhaus, *Phys. Rev.* **B39**, 804 (1989)).